A BCool magnetic snapshot survey of solar-type stars

S. C. Marsden,[1]★ P. Petit,[2,3]★ S. V. Jeffers,[4]★ J. Morin,[4,5] R. Fares,[6] A. Reiners,[4]
J.-D. do Nascimento Jr,[7,8] M. Aurière,[2,3] J. Bouvier,[9] B. D. Carter,[1] C. Catala,[10]
B. Dintrans,[2,3] J.-F. Donati,[2,3] T. Gastine,[11] M. Jardine,[6] R. Konstantinova-Antova,[12]
J. Lanoux,[2,3] F. Lignières,[2,3] A. Morgenthaler,[2,3] J. C. Ramìrez-Vèlez,[13] S. Théado,[2,3]
V. Van Grootel[14] and the BCool Collaboration[14]

[1]*Computational Engineering and Science Research Centre, University of Southern Queensland, Toowoomba 4350, Australia*
[2]*Institut de Recherche en Astrophysique et Planétologie, Université de Toulouse, UPS-OMP, F-31400 Toulouse, France*
[3]*CNRS, Institut de Recherche en Astrophysique et Planétologie, 14 Avenue Edouard Belin, F-31400 Toulouse, France*
[4]*Institut für Astrophysik, Georg-August-Universität Göttingen, Friedrich-Hund-Platz 1, D-37077 Göttingen, Germany*
[5]*LUPM-UMR 5299, CNRS & Université Montpellier II, Place Eugène Bataillon, F-34095 Montpellier Cedex 05, France*
[6]*SUPA, School of Physics & Astronomy, University of St Andrews, North Haugh, St. Andrews, KY16 9SS, UK*
[7]*Departamento de Fisica Teórica e Experimental, Universidade Federal do Rio Grande do Norte, CEP 59072-970 Natal, RN, Brazil*
[8]*Harvard–Smithsonian Center for Astrophysics, Cambridge, MA 02138, USA*
[9]*UJF-Grenoble 1/CNRS-INSU, Institut de Planétologie et d'Astrophysique de Grenoble (IPAG) UMR 5274, F-38041 Grenoble, France*
[10]*Observatoire de Paris, LESIA, 5 place Jules Janssen, F-92195 Meudon Cedex, France*
[11]*Max Planck Institut für Sonnensystemforschung, Max Planck Strasse 2, D-37191 Katlenburg-Lindau, Germany*
[12]*Institute of Astronomy and NAO, Bulgarian Academy of Sciences, 72 Tsarigradsko shose, BG-1784 Sofia, Bulgaria*
[13]*Instituto de Astronomia, Universidad Nacional Autonoma de Mexico, 04510 Coyoacan, DF, Mexico*
[14]*Institut dAstrophysique et de Géophysique, Université de Liege, Allée du 6 Aout 17, B-4000 Liege, Belgium*

ABSTRACT

We present the results of a major high-resolution spectropolarimetric BCool project magnetic survey of 170 solar-type stars. Surface magnetic fields were detected on 67 stars, with 21 classified as mature solar-type stars, a result that increases by a factor of 4 the number of mature solar-type stars on which magnetic fields have been observed. In addition, a magnetic field was detected for 3 out of 18 of the subgiant stars surveyed. For the population of K-dwarfs, the mean value of $|B_l|$ ($|B_l|_{\rm mean}$) was also found to be higher (5.7 G) than $|B_l|_{\rm mean}$ measured for the G-dwarfs (3.2 G) and the F-dwarfs (3.3 G). For the sample as a whole, $|B_l|_{\rm mean}$ increases with rotation rate and decreases with age, and the upper envelope for $|B_l|$ correlates well with the observed chromospheric emission. Stars with a chromospheric S-index greater than about 0.2 show a high magnetic field detection rate and so offer optimal targets for future studies. This survey constitutes the most extensive spectropolarimetric survey of cool stars undertaken to date, and suggests that it is feasible to pursue magnetic mapping of a wide range of moderately active solar-type stars to improve our understanding of their surface fields and dynamos.

Key words: line: profiles – magnetic fields – stars: activity.

1 INTRODUCTION

For the Sun and other slowly rotating solar-type stars, an interface-layer dynamo operating at the tachocline between the radiative and convective zones qualitatively explains the generation of toroidal and poloidal fields, the presence of a solar activity cycle and the strong dependence of activity on stellar rotation (Parker 1955; Charbonneau 2010), although there remain many aspects of solar magnetic field generation that cannot be comprehensively modelled or fully understood. For solar-type stars that rotate much faster than the modern-day Sun, the dynamo appears to be generated by a fundamentally different type that operates throughout the whole convection zone, a so-called distributed dynamo whose existence is supported by the observational evidence accumulated throughout the last decade (e.g. Donati et al. 2003; Petit et al. 2004; Marsden et al. 2006) and detailed numerical models (Brown et al. 2010). To

★ E-mail: marsden@usq.edu.au (SCM); ppetit@irap.omp.eu (PP); jeffers@astro.physik.uni-goettingen.de (SVJ)

better understand dynamos across a range of solar-type stars and their evolution with the star, the observation of a variety of active stars offers an efficient way to probe how various physical stellar parameters (especially the depth of the convective zone or the rotation rate) can enhance or inhibit dynamo processes.

Improved understanding of how the stellar dynamo operates in solar-type stars can be sought by probing the magnetic fields of cool stars across a range of stellar properties. However, most techniques used to observe stellar magnetism either involve indirect proxies, such as Ca ɪɪ H&K, X-ray and radio measurements, or have involved a small number direct measurements obtained from Zeeman broadening (see Reiners 2012, for a review). Despite these limitations, these surveys have shown a clear rotational dependence and saturation of the stellar dynamo, a relationship between stellar magnetic cycles and stellar rotation period, and a tight correlation between dynamo efficiency and Rossby number (e.g. Saar 2002; Böhm-Vitense 2007).

One of the most insightful ways to observe the dynamo in solar-type stars is through the use of spectropolarimetric observations. A significant amount of work has previously been achieved using spectropolarimetric observations of young, active, solar-type stars (e.g. Donati et al. 1997, 2003; Jeffers et al. 2011; Marsden et al. 2011a,b), but it is only with recent advances in instrumentation, such as the development of the ESPaDOnS and NARVAL spectropolarimeters, that it is possible to directly measure solar strength magnetic fields on stars other than the Sun. This approach is complementary to other magnetic field proxies, since polarimetry is providing us with information on the strength and polarity of the large-scale magnetic field component.

The BCool[1] project is an international collaboration of over 70 scientists with a common goal of understanding the magnetic activity of low-mass stars. The BCool project approaches this question from both theoretical and observational viewpoints and has a number of threads of investigation, ranging from understanding how fully convective stars generate magnetic fields in the absence of an interface layer (e.g. Donati et al. 2006a; Morin et al. 2008) through to determining if the magnetic field in evolved stars has a fossil or dynamo origin (e.g. Konstantinova-Antova et al. 2012). In this paper, we present the first large-scale spectropolarimetric survey of active and inactive solar-type stars to help our understanding of how the magnetic dynamo operates in solar-type main-sequence F-, G- and K-stars as part of the BCool cool star thread.

There are three main aspects to this BCool project studies of solar-type stars: (1) a snapshot survey of a large number of solar-type stars, in order to determine the number of stars showing detectable magnetic fields and how the properties of these magnetic fields change with basic stellar parameters (this paper). (2) For a sample of interesting stars from the snapshot survey, we have embarked on a programme to obtain maps of their global magnetic topology (e.g. Waite et al. 2014; Petit et al., in preparation). (3) For a further, even smaller, stellar sample, we have undertaken long-term mapping, in order to look for stellar activity cycles (e.g. Petit et al. 2009; Morgenthaler et al. 2012; Boro Saikia et al. 2014; Jeffers et al. 2014).

The snapshot survey, which is the focus of this paper, has two main aims: (1) to detect magnetic fields on our target sample of stars so that we can select the most suitable targets for long-term mapping of their magnetic field topology and (2) to determine if the large-scale magnetic field properties of solar-type stars vary with

basic stellar parameters, such as age, temperature, rotation rate and Ca ɪɪ H&K emission. Additionally, this paper aims to determine if the detection rate of magnetic fields varies significantly with the signal-to-noise ratio of the observations (i.e. is there a minimum signal-to-noise ratio required to detect a magnetic field) and what is the minimum Ca ɪɪ H&K S-index for which we can get magnetic detections (i.e. is the S-index a good proxy for magnetic field detections).

In this paper, we first describe the target selection and the spectropolarimetric observations in Sections 2 and 3. In Sections 4 and 5, we detail the analysis undertaken on the data set and in Section 6 we discuss the results of the survey.

2 THE BCool SAMPLE

The goal of the BCool spectropolarimetric survey is to observe as many of the bright ($V \lesssim 9.0$) solar-type stars as possible to further our understanding of the magnetic activity of cool stars. In this first paper, we present the spectropolarimetric snapshots of 170 solar-type stars that we have observed starting in 2006 until 2013 as part of the BCool survey. The initial targets were chosen from the Valenti & Fischer (2005) SPOCS (Spectroscopic Properties of Cool Stars) catalogue as they have accurate values for their stellar parameters. Since Valenti & Fischer (2005) mainly focused on G-dwarfs, our target list shows a dearth of both F- and K-stars. To address this observational bias, 10 additional K-stars were included from the Wright et al. (2004) catalogue, and other sources as specified in Table 1, mostly based on their higher activity levels which introduced a bias towards younger K-stars. Additionally, stars that are already known to show magnetic cycles were included from Baliunas et al. (1995) together with a sample of stars of around solar mass of varying ages to represent the Sun across its evolutionary path (see references in Table 1). Most of the stars in our sample are mature solar-type stars, but there is a large spread in ages (Table 1).

The stellar parameters for each star are summarized in Table 1. For most stars, the stellar parameters of the targets were taken from either Valenti & Fischer (2005) or Takeda et al. (2007a). For the remaining ~20 per cent of our sample, the stellar parameters are taken from other papers, as indicated in Table 1. The Rossby number in Table 1 was calculated for each star using the formulations of Wright et al. (2004, equation 13) which relates the chromospheric activity, $\log(R'_{HK})$, of the star to its Rossby number. The $\log(R'_{HK})$ values used for this calculation are the individual measurements from this paper, see Section 5.1.

Using the stellar parameters given in Table 1 and directly extracted from our input catalogues, we placed the stars contained in the BCool sample on a Hertzsprung–Russell (HR) diagram, which is shown in Fig. 1 (upper panel). The BCool sample predominantly contains dwarf stars, but a number (18) of subgiant stars have also been observed as part of the programme. The HR diagram was used to classify our stars as either dwarfs or subgiants using the dashed line shown in Fig. 1. All stars in our sample have a T_{eff} measure; however, there are eight stars for which we do not have any luminosity information, and thus are not included in Fig. 1. For these eight stars, six have $\log(g)$ values of greater than 4.0 cm s^{-2} and are thus classified as dwarfs, while a seventh (HIP 109647) has a $\log(g)$ value below 4.0 cm s^{-2} and has thus been classified as a subgiant. The last target (HIP 38018) has neither $\log(g)$ nor luminosity information, but we have assumed that it is a dwarf based on its radius ($1.157^{+0.079}_{-0.079}$ R$_\odot$; Masana et al. 2006). Using the simple radius and temperature relationship to luminosity, this radius, along with $T_{eff} = 5476$ K, gives a luminosity of $\log(Lum) = +0.033$,

Table 1. The stellar parameters of the BCool solar-type star sample. The fifth column gives the spectral type of the star according to SIMBAD (http://simbad.u-strasbg.fr/Simbad, Wenger et al. 2000). The 13th column gives the radius of the stellar convective zone, while the last two columns give the log of the Rossby number [calculated from equation 13 of Wright et al. (2004) from the individual log(R'_{HK}) measurements see Section 5.1] and the list of references (see the footnote at the end of the table) where the data have been taken from. SG: identifies a star as a subgiant, see Fig. 1 and B indicates a possible binary with two stars seen in the Stokes I LSD profile (the analysis has been done on the deeper of the two Stokes I profiles). X indicates an undetermined parameter. The complete version of this table is in the electronic edition of the journal. The printed edition contains only a sample.

HIP no.	SPOCS no.	HD no.	Other names	Sp. Type	T_{eff} (K)	$\log(g)$ (cm s^{-2})	$\log(M/H)$ or $\log(Fe/H)$*	$\log(Lum)$ ($L_\odot$)	Age (Gyr)	Mass ($M_\odot$)	Radius ($R_\odot$)	Radius$_{CZ}$ ($R_\odot$)	$v\sin i$ (km s^{-1})	log (Rossby number)	Refs.
400	1	225261	–	G9V	5265^{+18}_{-18}	$4.54^{+0.04}_{-0.02}$	$-0.31^{+0.03}_{-0.03}$	$-0.341^{+0.049}_{-0.049}$	$12.28^{+1.72}_{-7.08}$	$0.794^{+0.034}_{-0.018}$	$0.80^{+0.02}_{-0.03}$	$0.240^{+0.010}_{-0.016}$	$0.0^{+0.5}_{-0.0}$	$+0.303^{+0.013}_{-0.009}$	1, 2
544	4	166	V439 And	K0V	5577^{+31}_{-31}	$4.57^{+0.01}_{-0.00}$	$+0.12^{+0.02}_{-0.02}$	$-0.215^{+0.023}_{-0.023}$	$0.00^{+0.84}_{-0.00}$	$0.977^{+0.010}_{-0.014}$	$0.88^{+0.02}_{-0.02}$	$0.254^{+0.007}_{-0.004}$	$4.1^{+0.4}_{-0.4}$	$-0.395^{+0.000}_{-0.004}$	1, 2
682	6	377	–	G2V	5873^{+44}_{-44}	$4.37^{+0.04}_{-0.04}$	$+0.11^{+0.03}_{-0.03}$	$+0.082^{+0.078}_{-0.078}$	$6.12^{+1.28}_{-1.48}$	$1.045^{+0.028}_{-0.024}$	$1.12^{+0.05}_{-0.05}$	$0.308^{+0.020}_{-0.021}$	$14.6^{+0.5}_{-0.5}$	$-0.395^{+0.000}_{-0.024}$	1, 2
1499	13	1461	–	G0V	5765^{+44}_{-44}	$4.37^{+0.03}_{-0.03}$	$+0.16^{+0.03}_{-0.03}$	$+0.078^{+0.041}_{-0.041}$	$7.12^{+1.40}_{-1.56}$	$1.026^{+0.040}_{-0.030}$	$1.11^{+0.04}_{-0.04}$	$0.323^{+0.019}_{-0.020}$	$1.6^{+0.5}_{-0.5}$	$+0.336^{+0.004}_{-0.004}$	1, 2
1813	16	1832	–	F8	5731^{+44}_{-44}	$4.28^{+0.04}_{-0.03}$	$-0.02^{+0.03}_{-0.03}$	$+0.119^{+0.074}_{-0.074}$	$10.88^{+1.36}_{-1.36}$	$0.965^{+0.020}_{-0.020}$	$1.18^{+0.06}_{-0.05}$	$0.365^{+0.021}_{-0.022}$	$2.8^{+0.5}_{-0.5}$	$+0.290^{+0.005}_{-0.000}$	1, 2
...															

References: 1: Valenti & Fischer (2005), 2: Takeda et al. (2007a), 3: Boyajian et al. (2012), 4: Wu et al. (2011), 5: Herrero et al. (2012), 6: Delfosse et al. (1998), 7: do Nascimento (private communication), 8: Holmberg, Nordström & Andersen (2009), 9: Bailer-Jones (2011), 10: Masana, Jordi & Ribas (2006), 11: Gonzalez, Carlson & Tobin (2010), 12: Santos, Israelian & Mayor (2004), 13: Ramírez, Meléndez & Asplund (2009), 14: Wright et al. (2011), 15: Yoss & Griffin (1997), 16: Martínez-Arnáiz et al. (2010), 17: Soubiran et al. (2008), 18: Affer et al. (2005), 19: Fernandes et al. (1998), 20: Balachandran (1990), 21: Takeda et al. (2005), 22: Strassmeier et al. (2003), 23: Takeda et al. (2007b), 24: Fuhrmann (1998), 25: do Nascimento, da Costa & De Medeiros (2010), 26: Luck & Heiter (2005), 27: Mishenina et al. (2012), 28: Ramírez et al. (2007) and 29: Casagrande et al. (2011).
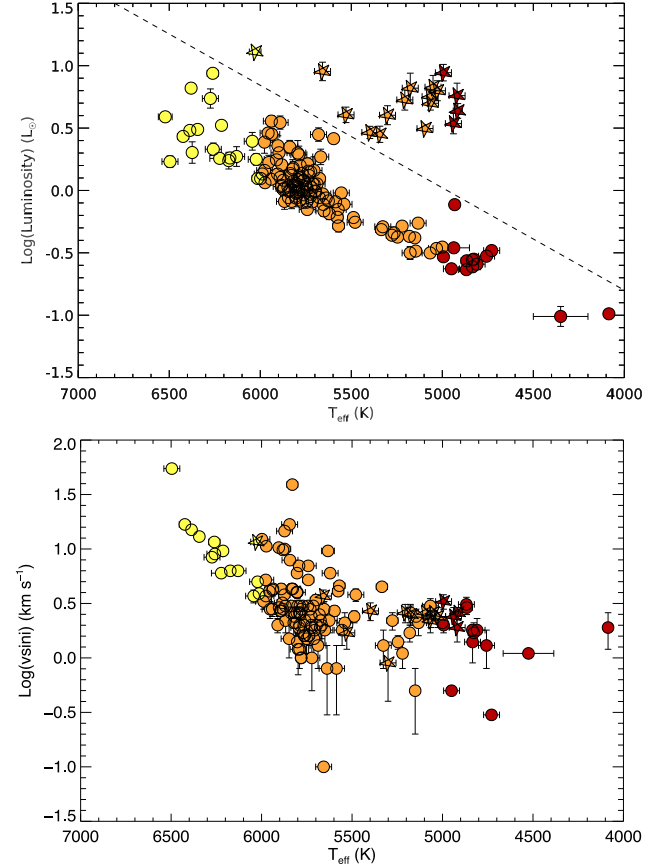

Figure 1. Plot of the HR diagram for our stars (upper panel) and a plot of log($v\sin i$) against effective temperature (lower panel). Stars in red have $T_{eff} < 5000$ K, those in orange have $5000 \leq T_{eff} \leq 6000$ K and those in yellow have $T_{eff} > 6000$ K. Filled circles represent dwarf stars and five-pointed stars represent subgiants, with the dividing line between the two shown as a dashed line (upper panel).

making HIP 38018 a dwarf according to Fig. 1. A plot of the $v\sin i$ values of the stars against their effective temperatures (Fig. 1, lower panel) shows that the mean rotation rate of the stars contained in the BCool sample decreases with a decreasing effective temperature. The mean $v\sin i$ value of the F-stars in the sample is significantly higher (12.0 km s^{-1}) than that of the G-stars (3.4 km s^{-1}) and the K-stars (1.8 km s^{-1}).

3 OBSERVATIONS

In this section, we describe the instrument and the observational procedure for securing the data and how the exposures are combined to produce Stokes I, Stokes V and N (null) profiles from the polarimetric sequence.

3.1 Polarimetric observations

3.1.1 Instrument description

The observations were secured with the Télescope Bernard Lyot (TBL; Observatoire du Pic du Midi, France) using the NAR-VAL echelle spectropolarimeter or with the Canada–France–Hawaii Telescope (CFHT; Mauna Kea, Hawaii) using the ESPaDOnS echelle spectropolarimeter with both instruments in polarimetric mode. NARVAL is a twin copy of ESPaDOnS and both have al-

most identical capabilities. The two spectropolarimeters provide full optical wavelength coverage (370–1000 nm) in a single exposure (with only a few nanometres missing in the near-infrared). The resolving power of both instruments is approximately 65 000, with a pixel size of 1.8 km s^{-1}, and both instruments comprise bench-mounted spectrographs that are fibre-fed from a Cassegrain-mounted polarimetric module. The polarimetric module consists of a series of three Fresnel rhombs that perform polarimetry over the entire spectral range. These are followed by a Wollaston prism which splits the incident light into two beams, each containing the opposite polarization state, which are then fed into the high-resolution spectrograph, so that both polarization states are recorded simultaneously. Thus, both Stokes *I* (unpolarized) and Stokes *V* (circularly polarized) spectra can be recovered from each observation. More information on the operation of NARVAL and ESPaDOnS can be found in Aurière (2003) and Donati et al. (2006b), respectively.

3.1.2 Observational procedure

Each Stokes *V* observation is obtained from a sequence of four subexposures. For each of these subexposures, the two half-wave rhombs are rotated (see Petit et al. 2003) so that the polarization state transmitted in each fibre is alternated, to help remove any instrumental effects. This results in the first and fourth and the second and third subexposures having the same polarization states being transmitted along the fibres. Consequently, each series of four subexposures results in eight spectra (four left-hand circularly polarized spectra and four right-hand circularly polarized spectra).

The intensity (Stokes *I*) spectrum is obtained by adding the eight spectra together, while the polarized (Stokes *V*) spectra is obtained by constructively adding the left-hand circularly polarized spectra and the right-hand circularly polarized spectra:

$$\frac{V}{I} = \frac{R_v - 1}{R_v + 1} \text{ where } R_v^4 = \frac{i_{1\perp}/i_{1\parallel}}{i_{2\perp}/i_{2\parallel}} \frac{i_{4\perp}/i_{4\parallel}}{i_{3\perp}/i_{3\parallel}} \qquad (1)$$

where $i_{k\perp}$ and $i_{k\parallel}$ are the two spectra obtained in subexposure *k*.

Additionally, a 'null' (*N*) spectrum is also computed to test for 'spurious' magnetic signatures. The null spectrum is created by destructively adding the left- and right-hand circularly polarized light and thus should cancel out any real magnetic signals:

$$\frac{N}{I} = \frac{R_n - 1}{R_n + 1} \text{ where } R_n^4 = \frac{i_{1\perp}/i_{1\parallel}}{i_{4\perp}/i_{4\parallel}} \frac{i_{2\perp}/i_{2\parallel}}{i_{3\perp}/i_{3\parallel}}. \qquad (2)$$

These formulas are from Donati et al. (1997) where more detail is given on the computation of *V*, *I* and *N* profiles from spectropolarimetric data.

3.2 Observations and data processing

The data for the BCool spectropolarimetric survey have been obtained over a total of 25 observing runs at TBL and CFHT starting in late-2006 and extending up to until mid-2013, with the vast majority of data being secured at the TBL. The journal of the observations including the number of observations for each star obtained at each observing epoch is given in Appendix B. Some of the stars (35/170 = 21 per cent) have been observed at multiple epochs to look for temporal evolution in their magnetic properties; however, the majority of the targets have only been observed once. The data were reduced using the LIBRE-ESPRIT data reduction package which is an automatic reduction software package that has been specifically designed for the reduction of spectropolarimetric observations. LIBRE-ESPRIT is based on ESPRIT which is described in Donati et al. (1997).

Table 2. Table of the stellar parameters covered by the LSD line masks.

Parameter	Range	Step size
T_{eff} (K)	4000–6500	250
log(g) (cm s^{-2})	3.5–4.5	0.5
log(M/H)	−0.2 to +0.2	0.2

For each stellar observation, both the Stokes *I* and *V* reduced spectra were computed with a sampling of 1.8 km s^{-1}.

3.3 Least-squares deconvolution

Because the S/N in the reduced spectra is not high enough to detect Zeeman signatures in individual lines, it was necessary to apply the least-squares deconvolution (LSD; Donati et al. 1997) technique to extract the polarimetric signal from the data. The LSD technique is a multiline technique that extracts the Stokes *I* and *V* information from each spectral line and builds one high signal-to-noise LSD profile. It is described in more detail in Donati et al. (1997) and Kochukhov, Makaganiuk & Piskunov (2010). LSD spectral profiles were computed for both the polarized and unpolarized spectra to produce both Stokes *V* and *I* LSD profiles for each observation with a resolved element of 1.8 km s^{-1}. To create LSD profiles, a line list or mask is generated from stellar atmosphere and spectral synthesis models for a set of stellar parameters similar to that of the observed star: T_{eff}, log(*g*) and log(M/H), with the range and step size of each of the three parameters given in Table 2. The model spectral lines are then selected based on central wavelength, central depth and Landé factor.

For the BCool snapshot survey, we created a grid of ∼100 model masks using the Vienna Atomic Line Database (VALD;[2] Kupka et al. 2000). The LSD line masks were created from VALD using all lines of depth greater than or equal to 10 per cent of the continuum. This is shallower than the minimum line depth that LSD traditionally uses (e.g. Donati et al. 1997), but several tests showed that the difference is compatible within the error bars. Strong lines such as the Ca II H&K and Hα lines were excluded from the line lists. The number of lines used in the calculation of the LSD profile ranges from 5200 to 14 700 depending on the stellar parameters, and the masks cover a wavelength range of 350–1100 nm. The number of lines used per LSD profile for each observation is tabulated in Table 3.

When creating the LSD profiles, the weighting of the spectral lines was adjusted so that the mean weight of both the Stokes *V* and Stokes *I* profile was close to unity. The formula used for determining the mean weights of the LSD profiles is given by

$$\text{Mean weight} = \frac{\sum_{j=1}^{n} S_j^2 w_j^2}{\sum_{j=1}^{n} S_j^2 w_j}, \qquad (3)$$

where *n* is the number of lines used to create the LSD profile, S_j is the signal-to-noise ratio and w_j is the line weight of the *j*th line given by

$$w_j = \frac{d_j \lambda_j g_j}{d_0 \lambda_0 g_0}, \qquad (4)$$

[2] http://vald.astro.univie.ac.at/~vald/php/vald.php

Table 3. Results from the analysis of the stellar LSD profiles of the BCool solar-type stars sample. Columns 2 and 3 give the observation date and observation number on that date. Columns 6 and 7 give the signal-to-noise ratio of the Stokes V LSD profile and the number of lines used to create the profile, while columns 8 and 9 note if there was a definite (D), marginal (M) or no (N) detection of a magnetic field in the profile along with the false alarm probability for the detection. Columns 10 and 11 give the velocity range over which equation (6) was calculated, while columns 12 and 13 give the measured B_l and N_l (equation 6) calculated using the null profile) measures. The final four columns give the total number of observations we have for each star and the number of definite, marginal and non-detections we have from these observations. N^D: indicates that the definite detection was unreliable due to noise and so a non-detection was chosen instead. SG: indicates a subgiant, see Fig. 1. VF: indicates that the previous radial velocity is from Valenti & Fischer (2005) rather than Nidever et al. (2002). NS: indicates a non-radial velocity standard star (i.e. $\sigma_{rms} \geq 100$ m s^{-1}) according to Nidever et al. (2002), all other stars with Nidever et al. (2002) radial velocities are considered to be radial velocity standard stars with $\sigma_{rms} < 100$ m s^{-1}. The complete version of this table is in the electronic edition of the journal. The printed edition contains only a sample.

HIP no.	Obs. date	Obs. no.	Obs. Rad. vel. (km s^{-1}) (this work)	Rad. vel. (km s^{-1}) (Nidever et al. 2002)	SNR$_{LSD}$	No. of lines used	Det?	FAP	v_{min} (km s^{-1})	v_{max} (km s^{-1})	B_l (G)	N_l (G)	Total no. of obs.	No. of def. det.	No. of mar. det.	No. of non-detections
400	10dec10	01	+7.7	+7.511	13 540	10 384	N	3.428×10^{-01}	-2	$+16$	$+2.1 \pm 1.0$	-0.3 ± 1.0	1	0	0	1
544	27sep10	01	-6.4	-6.537	45 559	12 137	D	$0.000 \times 10^{+00}$	-16	$+4$	$+2.7 \pm 0.3$	-0.2 ± 0.3	1	1	0	0
682	13dec10	01	+1.5	+1.184	18 853	11 135	D	7.377×10^{-06}	-16	$+18$	$+4.4 \pm 1.8$	-0.6 ± 1.8	1	1	0	0
1499	19oct10	01	-10.0	-10.166	23 795	11 140	N	6.059×10^{-01}	-18	-2	-0.6 ± 0.5	-0.6 ± 0.5	1	0	0	1
1813	03jan11	01	-30.4	-30.550	22 433	9712	N	4.001×10^{-02}	-40	-20	$+2.4 \pm 0.7$	$+0.0 \pm 0.7$	1	0	0	1
...																

^{a}Magnetic detection uncertain as a significant signal is also evidenced in the null profile (N_l).

Table 4. The normalization parameters used to create the LSD profiles for every 250 K step in T_{eff}.

T_{eff} (K)	d_0	λ_0	g_0
4000	0.55	650.0	1.22
4250	0.55	640.0	1.22
4500	0.55	630.0	1.22
4750	0.55	620.0	1.22
5000	0.54	610.0	1.22
5250	0.54	600.0	1.22
5500	0.53	590.0	1.22
5750	0.52	580.0	1.22
6000	0.51	570.0	1.22
6250	0.50	570.0	1.21
6500	0.49	560.0	1.21

for Stokes V data and by

$$w_j = \frac{d_j}{d_0}, \tag{5}$$

for Stokes I data, where d is the line central depth, λ is the line central wavelength and g is the line's Landé factor. The values of d_0, λ_0 and g_0 are the normalization parameters and were varied for every 250 K step in effective temperature and are given in Table 4.

For each Stokes V and I LSD profile, the line mask that matches most closely to each star's parameters [T_{eff}, $\log(g)$ and $\log(M/H)$] from Table 1 is used. For several stars without $\log(g)$ or $\log(M/H)$ values, $\log(g) = 4.5$ cm s^{-2} and $\log(M/H) = 0.00$ was used and $\log(Fe/H)$ was substituted for $\log(M/H)$ where a star had only a $\log(Fe/H)$ measurement. In the BCool snapshot sample, there are four stars that have metallicities far outside the range shown in Table 2. For these stars (HIP 17147, HIP 32851, HIP 57939, HIP 91043), individual line masks were created. However, the use of different metallicities was found to be of no significance. Examples of the LSD profiles of some of the more widely known targets are given in Appendix A along with more detailed notes on these stars.

4 THE LONGITUDINAL MAGNETIC FIELD, B_l

A star's surface magnetic field can be measured directly from the stellar Stokes V and I LSD profiles. This results in a value for the mean longitudinal magnetic field (B_l, which can also be referred to as $\langle B_z \rangle$), where B_l is the line-of-sight component of the stellar magnetic field integrated over the visible stellar disc. Because the LSD profiles are in velocity space (v), we can determine B_l from the first-order moment of the Stokes V LSD profile using (Mathys 1989; Donati et al. 1997):

$$B_l = -2.14 \times 10^{11} \frac{\int vV(v)\mathrm{d}v}{\lambda_0 g_0 c \int [I_c - I(v)]\mathrm{d}v}, \tag{6}$$

where B_l is in gauss, λ_0 and g_0 are given in Table 4 and c is the speed of light in km s^{-1}. I_c is the continuum level of the intensity profile and as this is normalized to 1.0, I_c is often replaced by 1.0 in some formulations of equation (6). The error in the measure of B_l (B_{err}) is determined by propagating the uncertainties computed by the reduction pipeline for each spectral bin of the normalized spectrum through equation (6).

We show in Fig. 2 the distribution of our observations as a function of the error bars in B_l estimates. The main factors affecting the uncertainties are the stellar $v \sin i$, the signal-to-noise ratio of the observation and the number of lines included in the LSD analysis as discussed in Shorlin et al. (2002). The majority of our measure-
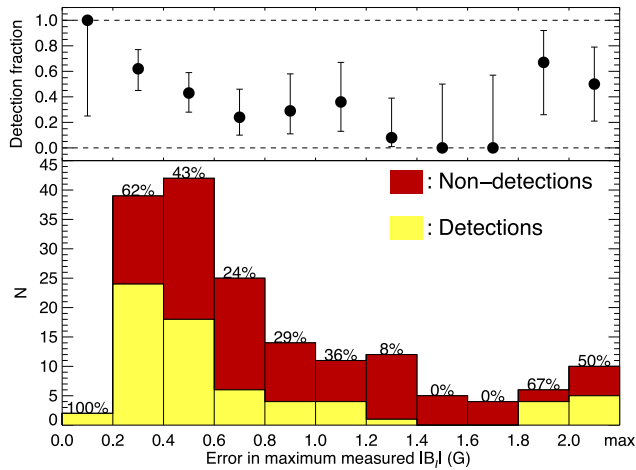
Figure 2. Histogram of detections/non-detections of surface magnetic fields against the error bar in B_l, using bins of 0.2 G. The detection rate (including both marginal and definite detections) for each bin is given above each column as a percentage, with the detection fraction (along with $\pm 2\sigma$ error bars) given in the upper panel.

Figure 3. Distribution of $|N_l|/\sigma_{N_l}$ measurements (ignoring measurements with $|N_l|/\sigma_{N_l} \geq 5$). The solid line represents the best fit of the data to a Gaussian function (giving an amplitude of 25.0773, a centroid of $-0.018\,516$ and $\sigma = 1.0667$). The dashed line is a Gaussian function of the same amplitude, but centred on zero and with $\sigma = 1$.

ments have error bars lower than 1 G, and the detection rates tend to be higher for measurements with the lowest uncertainties.

An additional source of uncertainty in measuring B_l is the determination of the velocity range over which to integrate equation (6). Calculations using a velocity range that is too narrow may result in the exclusion of polarized signal, while using a velocity range that is too wide could result in the introduction of additional noise, and possibly spurious polarization signal, to the measurement. For stars with definite strong magnetic detections, the width over which to integrate equation (6) can be determined from the presence of a well-defined Stokes V profile. However, most of the stars in our sample have no magnetic detection in their Stokes V LSD profiles, so it was necessary to use a more robust technique for the entire data set. We initially calculated B_l over a range of velocity widths and chose the width for which the ratio of $|B_l|/B_{err}$ is maximized as this should minimize the amount of noise in our measurement of B_l. This was performed on each observation of the BCool sample. For stars with multiple observations, only the observation with the largest value of $|B_l|$ was chosen to be analysed and to be presented in this paper. This is because the upper envelope of $|B_l|$ values are the most relevant, see Section 6.3. For stars with no strong magnetic detection, the measure of B_l is likely to be an upper estimate due to the noise contained in the Stokes V profile.

For each star, the value of B_l, the velocity ranges over which B_l was calculated and the magnetic field measured from the null profile (N_l) are presented in Table 3. For most stars, the value of N_l is near zero, which is consistent with a magnetic field measurement unaffected by spurious polarization signals. However, in a number of observations the N_l value diverges from zero by more than 3σ. In these cases, the magnetic field detection can still be considered as robust if $|N_l|$ is small compared to $|B_l|$, although the statistical error bar given on B_l is then likely underestimating the true uncertainty on the measurement. If $|N_l|$ is significantly greater than zero and is significant compared to $|B_l|$, the magnetic field estimate should be considered with great care. We note that other activity indicators deduced from the same observation and listed in the present study are unaffected by this issue.

To further evaluate the robustness of polarimetric measurements performed on our stellar sample, we adopt the method proposed
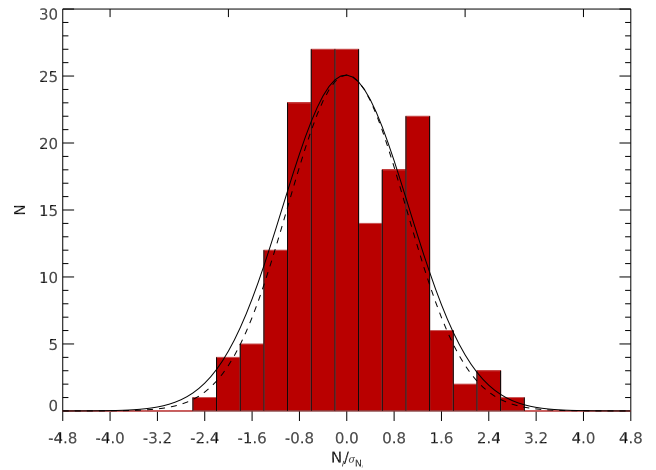
by Bagnulo et al. (2012) and plot in Fig. 3 the distribution of N_l measurements normalized by their statistical error bar (ignoring by default our five measurements with $|N_l|/\sigma_{N_l} \geq 5$). The adjustment of a Gaussian function on the distribution gives a centroid close to zero and $\sigma \approx 1$ (note that the inclusion of data points with $|N_l|/\sigma_{N_l} \geq 5$ does not significantly alter this result). This outcome suggests that N_l measurements are actually dominated by photon noise, which gives further support to the usefulness of N_l/σ_{N_l} measurements to help discriminate between reliable and more uncertain field measurements.

Table 3 also lists the observation date (of the analysed observations) and the radial velocity of the star as measured by this work and previous works (Nidever et al. 2002; Valenti & Fischer 2005). Additionally, Table 3 shows the signal-to-noise ratio of the Stokes V LSD profile for the chosen observation, the number of spectral lines used in the computation of the LSD profile, if there was a magnetic field detected on the star and the false alarm probability (FAP) of the magnetic field detection. Finally, Table 3 also lists the total number of observations for each star, the number of definite detections, marginal detections and null detections of a magnetic field; see Section 4.1 for the definition of definite and marginal detections.

4.1 False alarm probability

In order to determine if any variations in a star's Stokes V LSD profile are due to a magnetic field or just noise, we determine the FAP for each observation. The FAP is based on a χ^2 probability function measured both inside and outside of the stellar spectral lines (as defined by the position of the Stokes I LSD profile). The FAP is determined for both the Stokes V and null LSD profiles with a definite detection (D) being defined as having an FAP smaller than 10^{-5} (i.e. a χ^2 probability of larger than 99.999 per cent), while a marginal detection (M) is defined as having an FAP less than 10^{-3} but greater than 10^{-5} (i.e. a χ^2 probability between 99.999 and 99.9 per cent); otherwise the detection is classified as a non-detection (N). For a definite or marginal detection, the signal must also be found within the line profile of the star (i.e. within $v_{rad} \pm v\sin i$). Further information on the evaluation of the FAP can be found in Donati, Semel & Rees (1992) and Donati et al. (1997).

4.2 Radial velocities

The radial velocities determined from this work (given in Table 3) were calculated by fitting a Gaussian profile to the unpolarized Stokes *I* LSD profile of each star and taking the centroid of the Gaussian as the radial velocity. As can be seen from Table 3, for those stars with previously measured radial velocities and known to be stable (see Nidever et al. 2002), our values are mostly within ± 0.3 km s^{-1} of those of Nidever et al. (2002).

5 STELLAR ACTIVITY PROXIES

In addition to the measurement of the magnetic field on the visible surface of each star, we also analysed more traditional measures of stellar activity, namely the emission in the Ca II H&K, Ca II infrared triplet (IRT) and Hα lines.

5.1 Ca II H&K emission

The most widely used activity proxy is a star's Ca II H&K emission. This has been used by a large number of authors and the Mount Wilson survey's S-index (cf. Baliunas et al. 1995) is a de facto standard for measuring Ca II H&K emission of solar-type stars. In order for our measurements to match the Mount Wilson S-index, we follow a similar method to that of Wright et al. (2004).

By early 2013, we had 113 stars in our sample in common with those of Wright et al. (2004) for which they had calculated the S-index. Of these 113 stars, we had 23 stars that were observed using ESPaDOnS on the CFHT and 94 stars that were observed using NARVAL on the TBL (with 4 stars being observed on both telescopes). For every intensity spectrum of these 113 stars, we removed all the overlapping orders from the reduced spectra from LIBRE-ESPRIT so that only the order containing the Ca II H&K lines (3933.663 and 3968.469 Å) remained. This order spanned from $\sim$3870 to $\sim$4020 Å for both spectrographs, thus easily covering the wavelength range required to calculate the S-index (see Wright et al. 2004, fig. 1). Unlike Morgenthaler et al. (2012), we did not re-normalize the spectra of each star before calculating the S-index as tests showed only minor differences in the calculation of the S-index when this was done. In order to determine the S-index for our stars, we followed the method of Wright et al. (2004) and determined the S-index by fitting:

$$\text{S-index} = \text{Ca}_{HK}\text{-index} = \frac{aF_H + bF_K}{cF_{R_{HK}} + dF_{V_{HK}}} + e, \qquad (7)$$

where F_H and F_K are the fluxes in 2.18 Å triangular bandpasses centred on the cores of the Ca II H&K lines, respectively, $F_{R_{HK}}$ and $F_{V_{HK}}$ are the fluxes in two rectangular 20 Å bandpasses centred on the continuum either side of the HK lines at 3901.07 and 4001.07 Å, see Wright et al. (2004, fig. 1) and a, b, c, d and e are coefficients to be determined.

In order to determine the coefficients from equation (7), we took every intensity spectrum of our 113 stars and calculated the flux through the H, K, R and V bandpasses. Then the mean values of F_H, F_K, F_R and F_V were calculated for each star (so as to minimize errors associated with temporal variations in stellar activity levels) and the coefficients of equation (7) were then adjusted, using a least-squares fit, so that the S-indices of our stars matched (as closely as possible given the different dates of observation) those from Wright et al. (2004). This was done separately for the NARVAL and ESPaDOnS observations and a good solution was found using the coefficients given in Table 5. A calculation of the coefficients for NARVAL was

Table 5. The coefficients for equation (7) we have determined for our NARVAL and ESPaDOnS observations.

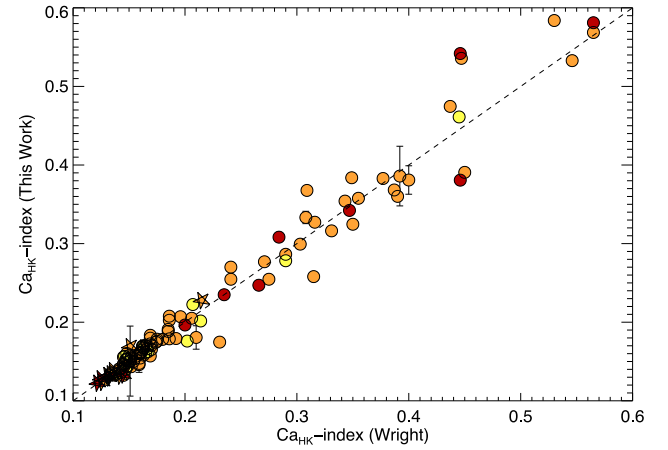| Coefficient	NARVAL	ESPaDOnS
a	12.873	7.999
b	2.502	-3.904
c	8.877	1.150
d	4.271	1.289
e	1.183×10^{-3}	-0.069

Figure 4. Plot of the S-index found in this work against that from Wright et al. (2004). The symbols are the same as in Fig. 1 with the dashed line representing a perfect match between the two measures.

previously done by Morgenthaler et al. (2012). However, this used a much smaller number of stars (31) and only used the Ca II H line. A plot of the S-index found from this project (using only the single observation for each star given in Table 3) to those from Wright et al. (2004) is given in Fig. 4.

The errors in the S-indices are an empirical estimate of the uncertainty in this single measurement and are calculated as the sample standard deviation of the S-indices of each of the four subexposures (see Section 3.1.2) of each observation. The S-indices were then converted to $\log(R'_{HK})$ using the formulations of Wright et al. (2004, equations 9–12), with the $B - V$ values for the stars coming from *Hipparcos* (Perryman et al. 1997) and Wright et al. (2004). The range in the $\log(R'_{HK})$ values given in column 6 of Table 6 gives the spread in $\log(R'_{HK})$ found from all observations of the star (ignoring the small error bars).

5.2 The calcium IRT and Hα emission

In addition to the Ca II H&K index, the activity of the stars was also analysed using the emission from the Ca II IRT lines at 8498.02, 8542.09 and 8662.14 Å, along with the emission in the Hα line (6562.85 Å). The Ca$_{IRT}$-index was calculated by using

$$\text{Ca}_{IRT}\text{-index} = \frac{F_{8498} + F_{8542} + F_{8662}}{F_{V_{IRT}} + F_{R_{IRT}}}, \qquad (8)$$

where F_{8498}, F_{8542} and F_{8662} are the fluxes measured in 2 Å rectangular bandpasses centred on the respective Ca II IRT lines, while $F_{V_{IRT}}$ and $F_{R_{IRT}}$ are the fluxes in 5 Å rectangular bandpasses centred

Table 6. The chromospheric activity of the BCool solar-type stars sample. Note that the chromospheric ages and rotation periods have been determined from the equations of Wright et al. (2004) from the individual log(R'_{HK}) measures rather than from the range of values. ^{SG}: indicates a subgiant, see Fig. 1. For the $(B − V)$ values, ^{W}: indicates a $(B − V)$ value from Wright et al. (2004). The complete version of this table is in the electronic edition of the journal. The printed edition contains only a sample.

HIP no.	$(B − V)$ (HIPP.)	S-index (Wright)	S-index (this work)	log(R'_{HK})	log(R'_{HK}) range	Chromospheric age (Gyr)	Chromospheric period (d)	Ca_{IRT}-index	Ca_{IRT}-index range	$H\alpha$-index	$H\alpha$-index range
400	0.755	0.174	0.1744 ± 0.0053	$-4.95^{+0.02}_{-0.03}$	-4.95	$4.664^{+0.537}_{-0.330}$	$35.3^{+1.1}_{-0.7}$	0.7976 ± 0.0045	0.7976	0.3046 ± 0.0004	0.3046
544	0.752	–	0.4591 ± 0.0015	$-4.36^{+0.00}_{-0.00}$	-4.36	$0.221^{+0.000}_{-0.000}$	$7.0^{+0.0}_{-0.0}$	0.8977 ± 0.0011	0.8977	0.3269 ± 0.0002	0.3269
682	0.626	0.377	0.3829 ± 0.0025	$-4.36^{+0.01}_{-0.00}$	-4.36	$0.221^{+0.000}_{-0.037}$	$4.3^{+0.0}_{-0.2}$	0.9238 ± 0.0009	0.9238	0.3183 ± 0.0004	0.3183
1499	0.674	0.156	0.1567 ± 0.0014	$-5.03^{+0.01}_{-0.01}$	-5.03	$6.214^{+0.221}_{-0.215}$	$29.0^{+0.3}_{-0.3}$	0.7149 ± 0.0016	0.7149	0.2908 ± 0.0001	0.2908
1813	0.639	0.170	0.1705 ± 0.0008	$-4.92^{+0.00}_{-0.01}$	-4.92	$4.178^{+0.157}_{-0.000}$	$22.1^{+0.2}_{-0.0}$	0.7372 ± 0.0013	0.7372	0.2867 ± 0.0002	0.2867
...											

on two continuum points, 8475.8 Å and 8704.9 Å, either side of the IRT lines. While the Hα-index was calculated using

$$\text{H}\alpha\text{-index} = \frac{F_{\text{H}\alpha}}{F_{V_{\text{H}\alpha}} + F_{R_{\text{H}\alpha}}}, \tag{9}$$

where $F_{\text{H}\alpha}$ is the flux in a 3.6 Å rectangular bandpass centred on the Hα line and $F_{V_{\text{H}\alpha}}$ and $F_{R_{\text{H}\alpha}}$ are the fluxes in two 2.2 Å rectangular bandpasses centred on the continuum points 6558.85 and 6567.30 Å. Equation (8) is taken from Petit et al. (2013, equation 1) while equation (9) is taken from Gizis, Reid & Hawley (2002, table 3).

The results of the Ca_{IRT}-index and Hα-index are given in Table 6, with once again the errors in the indices being calculated from the standard deviation of the measurements from the four subexposures and the range of the indices being the range seen over all of the multiple observations of a star (again ignoring the small error bars).

6 RESULTS AND DISCUSSION

6.1 Longitudinal field measurements

One of the unique results that can be obtained from spectropolarimetric observations is a measure of the mean longitudinal magnetic field (B_l) on the visible stellar surface (equation 6). One goal of this paper is to investigate how B_l varies with basic stellar parameters, such as T_{eff}, age and rotation rate, as well as how it relates to other more traditional activity proxies.

Unlike the traditional activity indicators (such as the S-index) which are sensitive to the magnetic field strength and therefore retain the contribution of most visible magnetic features, the measured longitudinal field is also sensitive to the field polarities. It is therefore very dependent upon the distribution and polarity mix of the magnetic regions across the stellar surface, and its value relates to the largest scale component of the magnetic field. Even in the most favourable case of a purely dipolar magnetic field, the value of B_l underestimates the polar field strength by at least a factor of 3 (Aurière et al. 2007). If the magnetic field distribution is more complex with different polarities across the visible hemisphere of the star (which is a likely situation with Sun-like stars), the measurement of B_l will even further underestimate the local stellar magnetic field strength.

As most of the stars in our sample have very low $v\sin i$ values, which makes the detection of complex magnetic fields especially difficult due to magnetic flux cancellation, this means that our measurements of the magnetic field are restricted to that of the large-scale field component on the stellar surface. However, a number of significant dynamo characteristics (e.g. magnetic cycles) are primarily expected to be seen on the largest spatial scales of the surface magnetic field. Thus, spectropolarimetric measurements are a useful probe of the underlying stellar dynamo, in spite of its intrinsically limited spatial resolution.

With this in mind, we have compared B_l to other activity indicators computed from the same spectra. As explained in Section 4, for stars with multiple observations we have chosen to analyse the observation that has given the largest absolute value of B_l, as this should correspond to a rotational phase that best represents the global magnetic field. It should be noted that this maximal value is still an underestimate of the local field strength in individual magnetic regions.

In the discussion of the results in following sections, we have broadly classified those stars with $T_{eff} < 5000$ K to be K-stars,

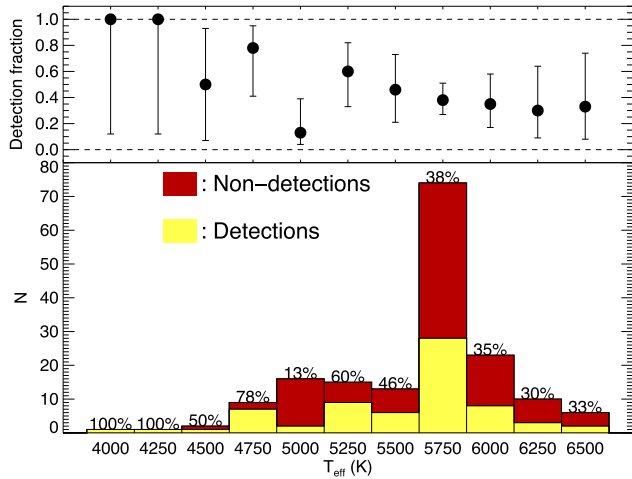**Figure 5.** Histogram of detections/non-detections of surface magnetic fields against T_{eff} for our BCool solar-type stars sample. The figure is as described in Fig. 2.

those with $5000 \leq T_{eff} \leq 6000$ K to be G-stars and those with $T_{eff} > 6000$ K to be F-stars.

6.2 Magnetic field detection rates

The overall detection rate of magnetic fields on the surface of our stars (including both marginal and definite detections) is 39 per cent (67 out of 170 stars) meaning that we have detected a magnetic field on 39 per cent of our stars, excluding multiple observations. There appears to be a slight increase in the detection rate for K-stars (12/21 = 57 per cent) over G-stars (49/130 = 38 per cent) and F-stars (6/19 = 32 per cent), but the numbers of K- and F-stars are quite small (compared to G-stars) and these percentages may be affected by statistical fluctuations or a selection bias (in particular their rotation or age, see discussions below). In Fig. 5, we have plotted the temperature distribution of our sample, showing the detection rate for each 250 K bin. This shows the strong bias towards stars around the solar temperature and the relative dearth of F- and K-stars in our sample.

6.2.1 Correlation with age

In Fig. 6, we have plotted the age distribution of our sample, showing the detection rate for each 1 Gyr bin. We consider two independent age estimates by taking ages computed by Takeda et al. (2007a) from evolutionary tracks (top panel) and chromospheric ages (bottom panel) calculated from our data, using the relation of Wright et al. (2004, equation 15) based on the individual measurements of $\log(R'_{HK})$ given in Table 6. A number of stars in Takeda et al. (2007a) have ages greater than recent estimates of the age of the Universe (Planck Collaboration I 2013), and we chose to ignore these stars in the plot, since some of the oldest objects are obviously much younger [Takeda et al. (2007a) actually acknowledge that their method produces an accumulation of stars with extreme ages]. A clear example is given by the visual binary system HD 131156, for which the primary component is estimated to be very young (less than 1 Gyr), while the secondary is listed with a much older age of 13 Gyr. In this case, the chromospheric ages come up with a more consistent overlapping estimate of 0.18–0.35 Gyr for the two companions (see Appendix A). Similarly, a number of stars
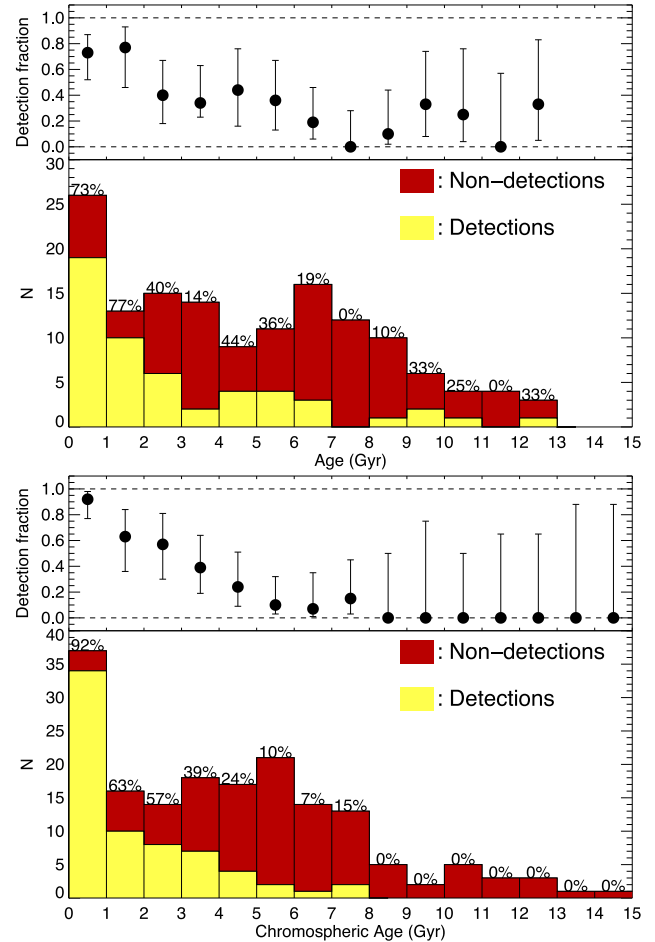

Figure 6. Histogram of detections/non-detections of surface magnetic fields against age (upper) and chromospheric age (lower), with the figure as described in Fig. 2. The chromospheric age has been determined from the Ca II H&K emission from Table 6 using Wright et al. (2004, equation 15).

in Takeda et al. (2007a) have estimated ages less than 0 Gyr and for these stars we have assigned an age of 0 Gyr.

As can be seen, our sample has a broad distribution of ages for stars up to at least 9 Gyr and the majority of our sample are mature aged solar-type stars. Fig. 6 shows that there is an unsurprisingly higher detection rate for younger stars, with stars around an age of 0–2 Gyr showing a detection rate of over 65 per cent. For stars older than ∼1–2 Gyr, the detection rate appears to drop, fluctuating between 0 and 57 per cent, with a smoother decrease in detection rate when the chromospheric age is considered.

The average age of all the stars in the sample, for which we have an age estimate from Takeda et al. (2007a, excluding those stars older than the age of the universe), is 4.8 Gyr (not taking into account the large error bars for each measurement). This value drops to 4.3 Gyr if chromospheric ages are used. For F-stars the average age is 2.4 and 3.0 Gyr (respectively for evolutionary tracks and chromospheric ages), while for G-stars it is 5.3 and 4.5 Gyr, and 2.7 and 4.4 Gyr for K-stars. Thus, the higher detection rates and activity seen on the K-stars (over that of the G-stars) in Figs 5 and 11 may be related to the youthfulness of the K-stars. However, a lower detection rate is obtained for F-stars (which are similarly young), suggesting that, at a given age, stellar large-scale magnetic fields are inversely correlated to the stellar mass.

Previously there have been very few magnetic field detections on mature solar-type stars, as stellar activity (and therefore magnetic field strength) declines significantly as a star ages. If we define mature as an age greater than 2 Gyr (ignoring the error bars in the age estimates), then one mature age solar-type star with a magnetic field detection was presented by Petit et al. (2008), HIP 79672 (18 Sco), which is part of this data set, while Fares et al. (2012) presented magnetic field detections and maps of the mature age planet-hosting star HD 179949. A further three mature age solar-type stars (HD 70642, HD 117207 and HD 154088) with magnetic detections were presented by Fossati et al. (2013). If we discard magnetic field detections on subgiant members of our sample, we have 21 mature age solar stars with magnetic field detections, 20 of which have not previously been reported.

6.2.2 Correlation with field strength

We plot in Fig. 7 field detections as a function of $|B_l|$ (yellow bins), and overplot non-detection (red bins) as a function of their upper limit on $|B_l|$. From this histogram, it is clear that it is virtually impossible to detect mean surface magnetic fields of less than $\sim$1 G on our stars even with the excellent signal-to-noise ratio of most of our observations, see Fig. 8 and Table 3 (the one detection for 0–1 G shown in Fig. 7 is for HIP 8362 with $B_l = -0.9 \pm 0.2$ G). Detection of surface magnetic fields of less than 1 G has been achieved previously for some cool stars (e.g. Aurière et al. 2009), but this has only been possible with the addition of a large number of spectropolarimetric observations. The detection rate correlates directly with the magnitude of the mean magnetic field. For field strengths of 5 G or greater, we obtain an almost 100 per cent detection rate. The few stars with fields greater than 5 G that did not give detections are due to the low signal-to-noise ratio of the observations ($SNR_{LSD} < 20\,000$).

6.2.3 Correlation with signal-to-noise

In Fig. 8, the sample magnetic field detection rate is plotted as a function of the signal-to-noise ratio of the Stokes V LSD profile. A significant majority (125/170 = 74 per cent) of our sample have observations with $SNR_{LSD} > 20\,000$. For those bins with five or

Figure 8. Histogram of detections/non-detections of surface magnetic fields against SNR_{LSD}, with the figure as described in Fig. 2.

more observations in them, Fig. 8 shows that the detection rate varies between 26 and 54 per cent with little evidence of an increase in the detection rate with an increase in SNR_{LSD}. This is mostly because longer exposure times were adopted for a number of low-activity targets with observations occasionally reaching $SNR_{LSD} > 50\,000$, but even this was not enough to detect the magnetic field on the surface of many mature low-activity Suns. Consequently, it is difficult to determine the lowest signal-to-noise ratio required to detect a surface magnetic field in any cool star, but given that the three stars with $|B_l|$ over 5 G that showed no detection have in common $SNR_{LSD} < 20\,000$, we adopt this value as the minimum signal-to-noise ratio to be aimed for in future observations.

6.2.4 Correlation with Ca H&K S-index

Fig. 9 shows the detection rate as a function of the Ca II H&K-index (S-index). Clearly from this plot, stars with an S-index $\gtrsim 0.2$ have a very high (77 per cent) rate of magnetic detection, while those stars with an S-index $\gtrsim 0.3$ are almost certain (89 per cent) to have a detectable magnetic field on the stellar surface, while for those stars with an S-index $\lesssim 0.2$ the probability of detecting a magnetic field is very low (11 per cent). The star with the smallest S-index which
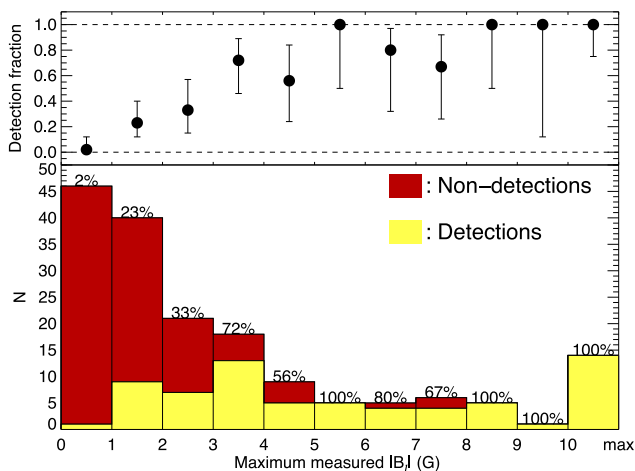

Figure 7. Histogram of detections/non-detections of surface magnetic fields against the maximum measured $|B_l|$, with the figure as described in Fig. 2. We emphasize that yellow bins (detections) correspond to actual field values, while red bins (non-detections) correspond to upper limits.
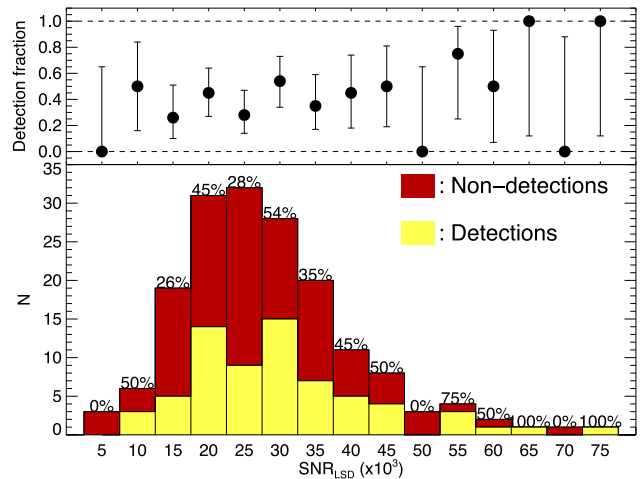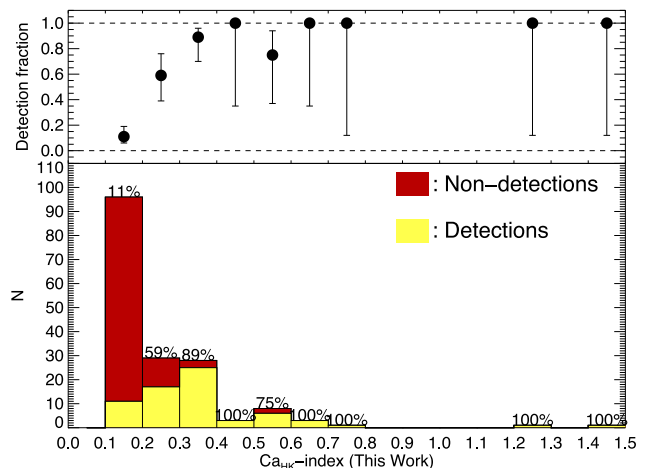

Figure 9. Histogram of detections/non-detections of surface magnetic fields against the Ca II H&K index, with the figure as described in Fig. 2.
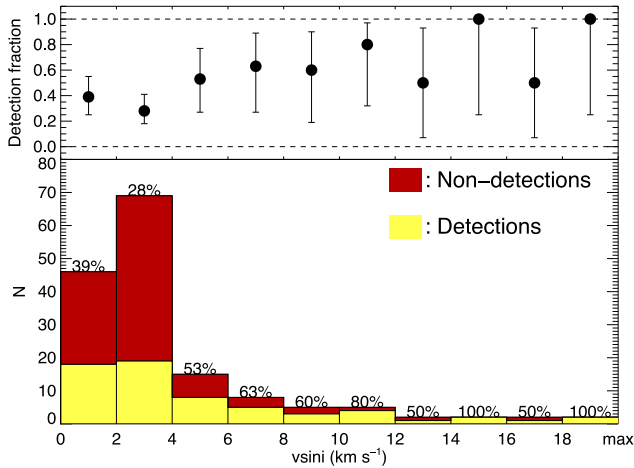
Figure 10. Histogram of detections/non-detections of surface magnetic fields against the stellar $v \sin i$, with the figure as described in Fig. 2.

shows a definite detection of a magnetic field is the subgiant HIP 113944 (S-index = 0.1677).

6.2.5 Correlation with v sin i

Fig. 10 shows the detection rate as a function of the $v \sin i$ of the star (with those stars with $v \sin i$ greater than 20 km s^{-1} being counted in the 18+ box). The detection rate for stars with $v \sin i$ values less than 4 km s^{-1} is 32 per cent (37/155) while for those stars with $v \sin i$ values between 4 and 10 km s^{-1} the detection rate is 57 per cent (16/28). For stars with $v \sin i$ values greater than 10 km s^{-1}, the detection rate increases to 77 per cent (10/13) with only three stars with $v \sin i$ values this high not giving magnetic detections.

6.3 The variation of $|B_l|$ with basic stellar parameters

Because the measurement of B_l is based on an averaged measure of the magnetic fields on the visible surface of a star, and because it is a measure of the amount of magnetic flux on the stellar surface, it is expected that B_l should show a correlation with other activity indicators (such as the Ca II H&K S-index). The shear scale of the large sample of stars with measured stellar parameters that we have in the BCool spectropolarimetric survey (from Valenti & Fischer 2005 and Takeda et al. 2007a) means that we can also investigate the relationship between $|B_l|$ and basic stellar parameters in a statistically significant manner.

In the following figures, we have only plotted those stars that have the relevant stellar parameters available (see Table 1). For stars with multiple observations (i.e. those that show a range in their measurements of activity in columns 6, 8 and 10 in Table 6), we have plotted the single measurement (i.e. the value from columns 4, 5, 7 and 9 in Table 6) that can be directly compared to the B_l measurement taken from the same observation (see Table 3).

6.3.1 Correlation with spectral type

A correlation of magnetic activity with stellar mass is commonly seen in activity indices, such as the S-index where for stars with similar ages, K-stars are generally more active than G-stars and G-stars are more active than F-stars (e.g. Noyes et al. 1984; Baliunas et al. 1995; Basri et al. 2010). It is therefore of particular
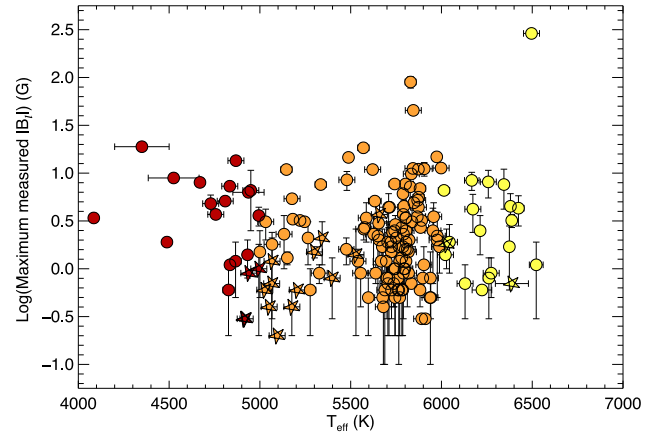

Figure 11. Plot of log(maximum measured $|B_l|$) against $T_{\rm eff}$. The symbols are the same as in Fig. 1.

interest to determine if K-stars also have stronger large-scale magnetic fields compared to G- and F-stars. In Fig. 11, we have plotted the maximum measured $|B_l|$ against the stellar effective temperature. This plot shows little evidence of a significant increase in the maximum field strength measured on K-stars compared to that seen on G-stars (ignoring the three most active stars in our sample, HIP 25486 [HR 1817], HIP 71631 [EK Dra] and HIP 91043 [V889 Her, HD 171488]) although there may be an indication of a weaker maximum field strength for F-stars. The mean $|B_l|$ measured on F-, G- and K-stars (excluding the subgiants and the three very active stars) is 3.3, 3.2 and 5.7 G, respectively, with the mean $|B_l|$ being 3.5 G. Thus, the mean measured field strength is somewhat higher for K-stars, compared to F- and G-stars. However, the number of main-sequence K-stars in our sample is comparatively small (17) and some of the K-dwarfs were specifically selected for our observations because they were known to be active stars. This may result in a bias towards stronger magnetic fields and bearing in mind that this bias is mostly equivalent to the bias towards low ages mentioned in Section 6.2.

6.3.2 Correlation with stellar age

When plotted against the stellar age, the maximum measured $|B_l|$ shows a general decrease in the upper envelope of the measured magnetic field strength as a star ages (see Fig. 12), similar to that observed in other activity indicators (e.g. Pace 2013). This trend is more pronounced when the chromospheric age is used and can be linked to the evolution with stellar age of the detection rate (see Fig. 6). The oldest stars of our list systematically display $|B_l|$ values of $\lesssim 5$ G, with an age limit that depends on the age determination method (around 7 Gyr from evolutionary models versus 4 Gyr from chromospheric emission). Using age values from Takeda et al. (2007a), HIP 114378 is a notable exception to the general trend with $|B_l|$ around 12 G (see Appendix A). We also note that most subgiants of our sample show up in the high-age tail of chromospheric ages, while their position is scattered at all ages using evolutionary tracks.

6.3.3 Correlation with stellar rotation

It is widely documented that the rotation rate of a star is tightly correlated to its stellar activity (e.g. Noyes et al. 1984). To understand if there is the same correlation with the large-scale magnetic
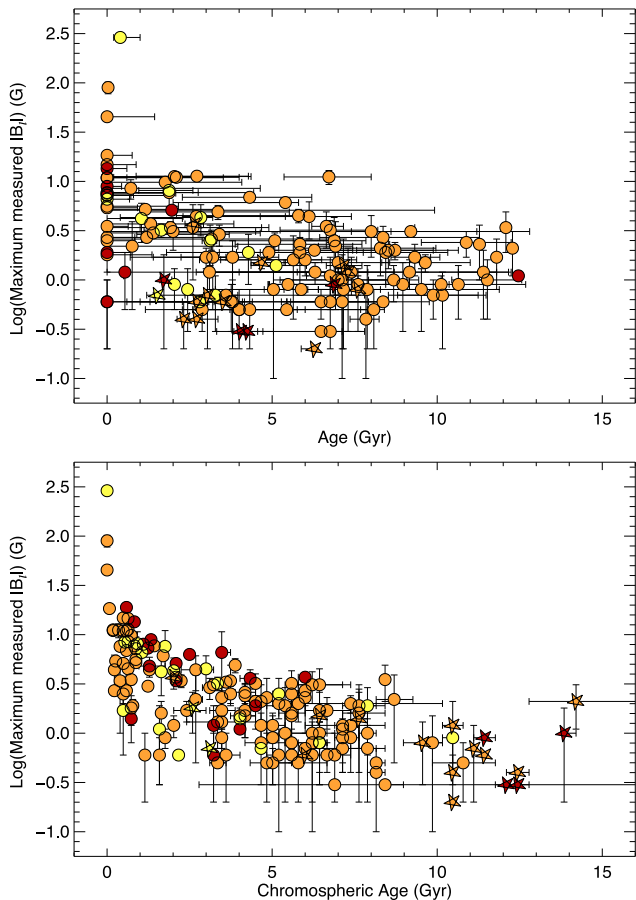
Figure 12. Plot of log(maximum measured $|B_l|$) against age (upper) and chromospheric age (lower), with the chromospheric age being determined as described in Fig. 6. The symbols are the same as in Fig. 1.

field strength, we used the projected rotational velocity as a proxy of stellar rotation (Fig. 13). The upper envelope of the $|B_l|$ values does appear to increase with rotation rate. We emphasize that, as a star's $v\sin i$ increases, the spatial resolution of the stellar surface also increases. This effect is however not expected to strongly bias the $|B_l|$ estimates, as the integrals in equation (6) cover the width of
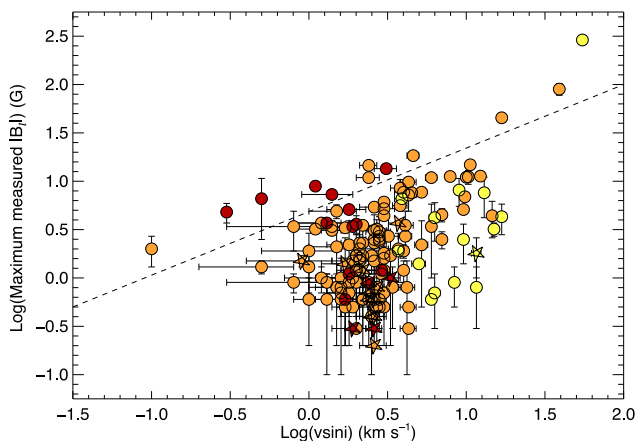
the Stokes profile and thus only measure the largest scale magnetic component, independently of the star's $v\sin i$ value.

There are a few stars which appear to have significantly larger $|B_l|$ values than other stars with similar $v\sin i$ values (shown above the dashed line in Fig. 13). Some of these deviant points are likely to be a result of an inclination effect where for a given rotation period, a low stellar inclination angle will result in a low $v\sin i$ value. A good example is HD 131156A, for which an inclination angle of 28° was proposed by Petit et al. (2005), in spite of a relatively rapid rotation of about 6 d. Several other deviant stars have been further studied using Zeeman–Doppler imaging (ZDI; Semel 1989) to reconstruct their large-scale surface magnetic topologies (Petit et al., in preparation). This allows an approximate determination of the stellar inclination angle by using the combined knowledge of the stellar radius, rotation period (estimated through the ZDI method) and $v\sin i$ value. For at least two of these stars (HIP 104214 and HIP 56997), the estimated stellar inclination angle is above 60° although it should be noted that they suffer from large error bars in the estimated inclination angle. We finally note that the 12 stars with higher $v\sin i$ values are mostly G- and K-dwarfs.

6.3.4 The mass–rotation plane

We also plot in Fig. 14 the distribution of the BCool sample in the mass–rotation plane. Stellar masses are taken from Takeda et al. (2007a), and rotation periods are derived from our S-index measurements, strictly following the prescription of Wright et al. (2004). Subgiants are removed from the plot (as their mass–temperature relationship is different from the one of main-sequence stars), as well as the three most active stars from our catalogue (HIP 25486 [HR 1817], HIP 71631 [EK Dra] and HIP 91043 [V889 Her, HD 171488]). With symbol sizes being proportional to the maximum measured $|B_l|$, this diagram highlights the sharp increase of surface magnetic field strengths towards lower masses and lower rotation periods, in overall agreement with similar diagrams shown in other studies (e.g. Donati & Landstreet 2009). It is obvious from this plot that, at a given rotation period, large-scale surface magnetic fields are much stronger in stars of lower mass (and therefore much
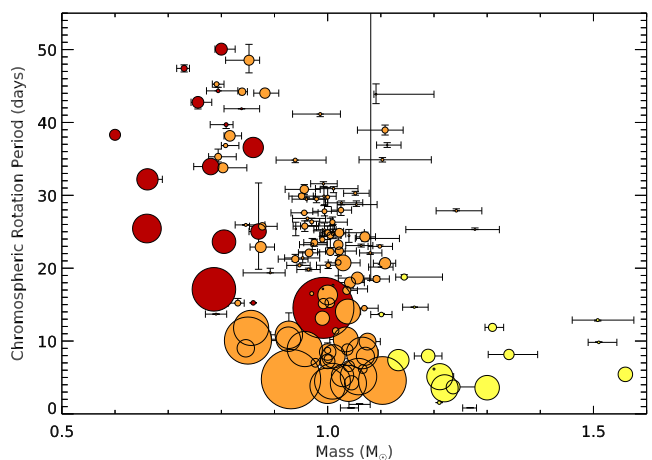

Figure 13. Plot of log(maximum measured $|B_l|$) against log($v\sin i$). The symbols are the same as in Fig. 1, with the stars above the dashed line being defined as having high $|B_l|$ values (see Section 6.3.3).

Figure 14. Distribution of BCool targets in the mass–rotation period plane. Symbol sizes are proportional to the maximum measured $|B_l|$. Note that subgiants were removed from this plot, as well as the three most active stars from our sample (HIP 25486 [HR 1817], HIP 71631 [EK Dra] and HIP 91043 [V889 Her, HD 171488]), due to their large symbol size that would affect the readability of the plot.

easier to detect). The upper-right part of the diagram, containing weakly magnetic stars, is free from any outlier displaying abnormally high magnetic field strength. The situation is different in the lower-left part of the plot where, among strongly magnetic objects, a few points reveal the presence of weak magnetic field measurements. These weakly magnetic outliers are stars that were observed only once during our survey, so that data may well have been taken at a rotational phase suffering from polarity cancellation. Future observations of these stars are necessary to confirm this hypothesis.

6.4 The correlation of $|B_l|$ with other stellar activity indicators

The maximum measured $|B_l|$ shows a clear correlation with other activity indicators (see Figs 15 and 16) with the upper envelope of $|B_l|$ increasing with the other activity indices. When plotted against the Rossby number, $|B_l|$ shows a similar increase to that of $\log(R'_{HK})$ taking note that the Rossby number has been determined using the formula from Wright et al. (2004, equations 13 and 14) which is based on the $\log(R'_{HK})$ value of the star. The outlying stars shown at low $v\sin i$ (see above) follow the general trend in this plot, confirming the hypothesis of an inclination effect to explain their relatively high surface magnetic fields.

We have extracted both the Ca II H&K and Ca II IRT emission from our observations, as described in Section 5.2. These two activity indicators have been observed simultaneously and are compared in Fig. 17, where they are seen to show a strong correlation. In contrast, the comparison of maximum measured $|B_l|$ with the Hα-index (Fig. 16) indicates a different trend. This is due to a strong
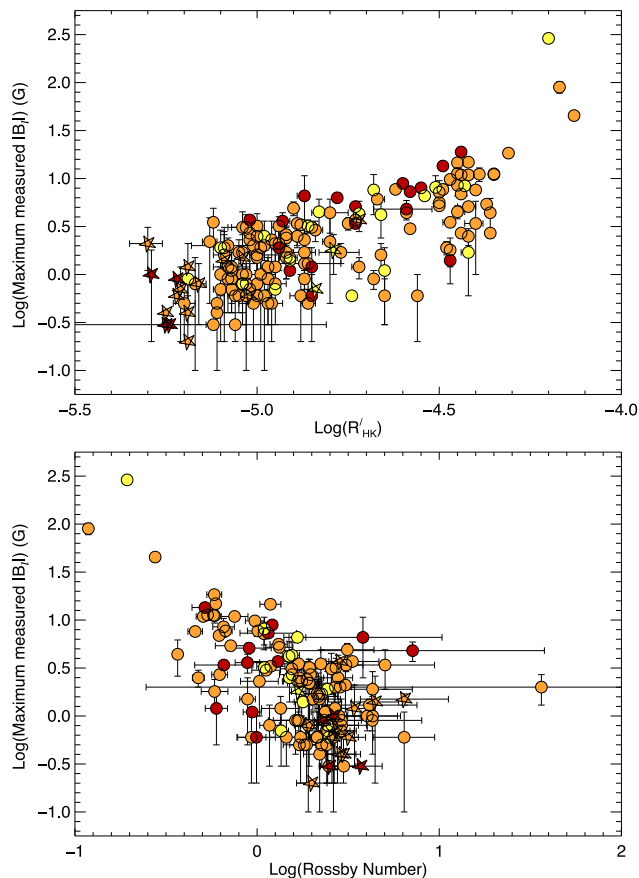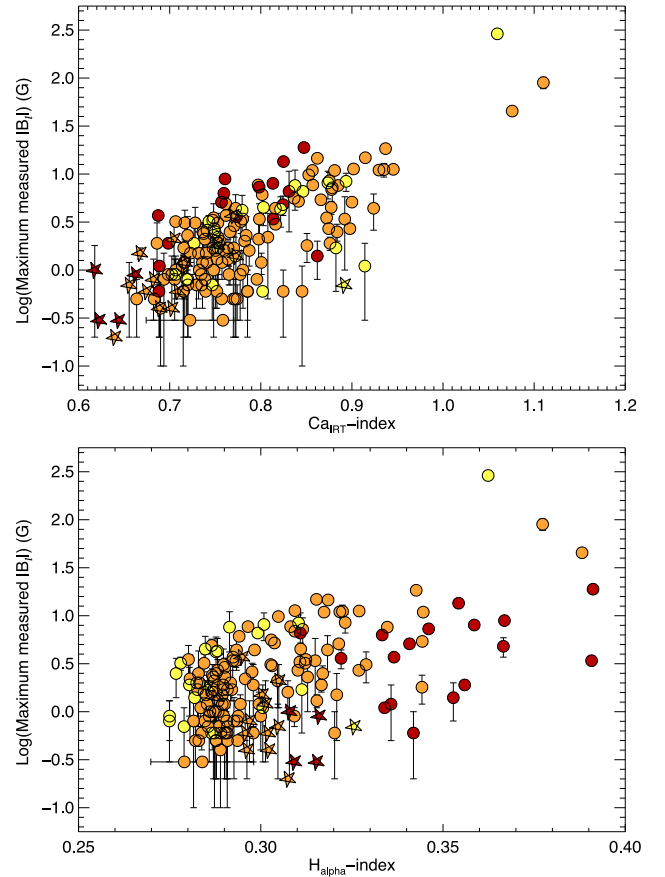

Figure 16. Plot of log(maximum measured $|B_l|$) against the Ca$_{IRT}$ activity index (top) and the Hα activity index (bottom). The symbols are the same as in Fig. 1.

Figure 15. Plot of log(maximum measured $|B_l|$) against $\log(R'_{HK})$ (top) and log(Rossby number) (bottom). The symbols are the same as in Fig. 1.

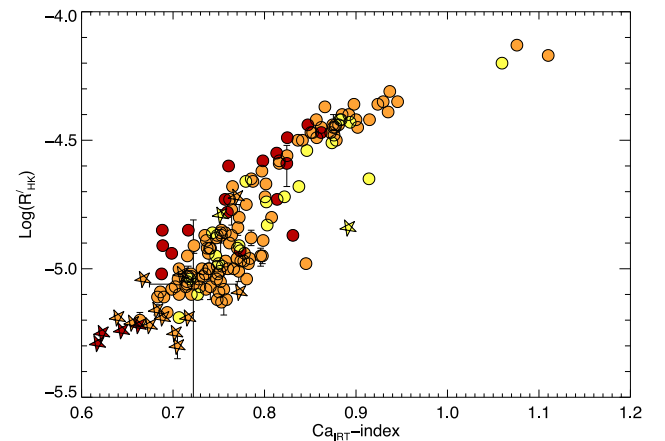**Figure 17.** Plot of $\log(R'_{HK})$ against the Ca$_{IRT}$ activity index. The symbols are the same as in Fig. 1.

temperature dependence for the Hα-index, where F-stars show a lower core emission than K-stars. This temperature dependence for Hα is consistent with previous studies by Bopp et al. (1988) and Strassmeier et al. (1990) and is not relevant for the other activity proxies [$\log(R'_{HK})$ and Ca$_{IRT}$-index].

6.5 The comparison with magnetic field measurements from Stokes *I* observations

As previously discussed, the measurements of $|B_l|$ from Stokes *V* (the large-scale field) reflect only a fraction of the average field on the star (measured in Stokes *I*). Observations of Stokes *I* and *V* have shown that typical values for the ratio between the large-scale field and the average field are of the order of 10 per cent or lower (Reiners, Basri & Browning 2009; Reiners 2012). From our sample, measurements of average field strengths from Stokes *I* are available for five stars: HIP 3765 (Marcy & Basri 1989), HIP 15457 (Saar & Baliunas 1992), HIP 16537, HIP 96100 (Valenti, Marcy & Basri 1995) and HIP 88972 (Basri & Marcy 1988); see Reiners (2012) for an overview and a discussion of different methods. In four of the five stars, measured average fields from Stokes *I* are around 200–300 G; only for HIP 96100 the field is lower with an upper detection limit of 100 G. The ratios between field strengths in Stokes *I* and *V* are below 7 per cent in all five stars. It should be noted that measurements in Stokes *I* and *V* were taken at different times in all cases. A significant systematic error in this fraction is therefore the variability of the field geometry visible at the time of observation (for both Stokes *I* and *V*).

7 CONCLUSIONS

One of the strongest threads of the BCool project is the study of main-sequence solar-type stars, aimed at understanding of how magnetic fields are generated in stars with physical parameters close to solar values. We have observed a large sample (170) of solar-type stars (on the main sequence or at the subgiant stage) using spectropolarimetric observations, in order to detect and characterize their surface magnetic fields. This data set will continue to expand and forms the basis of the BCool solar-type star sample, on a subsample of which further analysis will be undertaken, such as the mapping of the magnetic topologies (Petit et al., in preparation) or long-term magnetic monitoring of specific targets in a search for magnetic cycles.

Prior to this paper, the majority of the magnetic field detections for solar-type stars have been achieved on young stars (e.g. Donati et al. 1997, 2003; Jeffers et al. 2011; Marsden et al. 2011a), with magnetic field detections for mature solar-type stars limited to only five such targets (Petit et al. 2008; Fares et al. 2012; Fossati et al. 2013). This project has detected magnetic fields on 67 stars from our stellar sample, with 21 of our stars with detections (and age estimates) being classified as mature age solar-type stars, 20 of which have not been reported previously, and so constituting a significant addition to previous studies.

Of the 18 subgiant stars that have been observed as part of the survey, we report a marginal detection of a surface magnetic field on one of the stars (HIP 5493) and definite detections of magnetic fields on two of them (HIP 109439 and HIP 113994). Further investigation is required to interpret these isolated magnetic detections on evolved objects for which slow rotation is expected and should lead to a low surface activity (as observed for the rest of the subgiants in our sample).

We have shown that for stars with a Ca II H&K S-index $\gtrsim 0.3$, we are almost certain to detect the presence of a magnetic field while for those stars with an S-index $\lesssim 0.2$ the detection rate falls to around 10 per cent, while the minimum signal-to-noise ratio required in the Stokes *V* LSD profile should be $> 20\,000$ to ensure a good detection rate. For stars with $|B_l| \gtrsim 5$ G, we are very likely to detect the surface magnetic field (given a reasonable signal-to-noise ratio) while for

stars with $|B_l| \lesssim 1$ G it is almost impossible to detect the surface magnetic field from individual measurements.

The results presented here indicate that the upper envelope of the absolute value of the mean longitudinal surface magnetic field ($|B_l|$) appears to be directly related to chromospheric activity indicators. The strength of B_l drops off with age and increases with rotation rate. The mean value of $|B_l|$ found from our measurements is 3.5 G, with K-stars having a higher mean $|B_l|$ (5.7 G) than F-stars (3.3 G) and G-stars (3.2 G), although the number of F- and K-stars in our sample is currently limited.

This paper presents an extensive and unique data set of the magnetic fields of solar-type stars, and a demonstration of the feasibility of more detailed follow-up studies. Subsequent mapping of the surface magnetic fields of a large number and wide range of these solar-type stars (including many Sun-like stars) would be of great scientific value, by providing an empirical basis for understanding how dynamos vary according to fundamental stellar properties, and may vary over time to produce magnetic cycles or other variability. In addition, magnetic maps would provide an empirical basis for the numerical modelling of stellar coronae and winds, and possible wind impacts on any orbiting planets (e.g. Vidotto et al. 2012). In overall terms, the magnetic detections presented here are thus likely to provide the basis for an extensive set of detailed magnetic studies that can provide fresh insights into the nature of stellar magnetism.

REFERENCES

Affer L., Micela G., Morel T., Sanz-Forcada J., Favata F., 2005, A&A, 433, 647
Anglada-Escudé G. Butler R. P., 2012, ApJS, 200, 15
Aurière M., 2003, in Arnaud J., Meunier N., eds, EAS Pub. Ser. Vol. 9, Magnetism and Activity of the Sun and Stars. p. 105
Aurière M. et al., 2007, A&A, 475, 1053
Aurière M. et al., 2009, A&A, 504, 231
Bagnulo S., Landstreet J. D., Fossati L., Kochukhov O., 2012, A&A, 538, A129
Bailer-Jones C. A. L., 2011, MNRAS, 411, 435
Balachandran S., 1990, ApJ, 354, 310
Baliunas S. L. et al., 1995, ApJ, 438, 269
Basri G., Marcy G. W., 1988, ApJ, 330, 274
Basri G. et al., 2010, ApJ, 713, L155
Benedict G. F. et al., 2006, AJ, 132, 2206
Böhm-Vitense E., 2007, ApJ, 657, 486
Bopp B. W., Dempsey R. C., Maniak S., 1988, ApJS, 68, 803
Boro Saikia S., Jeffers S. V., Petit P., Marsden S., Morin J., 2014, A&A, submitted
Boyajian T. S. et al., 2012, ApJ, 757, 112
Brown B. P., Browning M. K., Brun A. S., Miesch M. S., Toomre J., 2010, ApJ, 7611, 424

Butler R. P. et al., 2006, ApJ, 646, 505

Casagrande L., Scönrich R., Asplund M., Cassisi S., Ramírez I., Meléndez J., Bensy T., Feltzig S., 2011, A&A, 530, A138

Charbonneau P., 2010, Living Rev. Sol. Phys., 7, 3

Delfosse X., Forveille T., Perrier C., Mayor M., 1998, A&A, 331, 581

do Nascimento J. D., Jr, da Costa J. S., De Medeiros J. R., 2010, A&A, 519, 101

Donati J.-F., Landstreet J. D., 2009, ARA&A, 47, 333

Donati J.-F., Semel M., Rees D. E., 1992, A&A, 265, 669

Donati J.-F., Semel M., Carter B. D., Rees D. E., Cameron A. C., 1997, MNRAS, 291, 658

Donati J.-F. et al., 2003, MNRAS, 345, 1145

Donati J.-F., Forveille T., Collier Cameron A., Barnes J. R., Delfusse X., Jardine M. M., Valenti J. A., 2006a, Science, 311, 683

Donati J.-F., Catala C., Landstreet J. D., Petit P., the ESPaDOnS Team, 2006b, in Casini R., Lites B. W., eds, ASP Conf. Ser. Vol. 358, Solar Polarization 4. Astron. Soc. Pac., San Francisco, p. 362

Fares R. et al., 2012, MNRAS, 423, 1006

Fernandes J., Lebreton Y., Baglin A., Morel P., 1998, A&A, 338, 455

Fossati L., Kochukhov O., Jenkins J. S., Stancliffe R. J., Haswell C. A., Elmasli A., Nickson E., 2013, A&A, 551, A85

Fuhrmann K., 1998, A&A, 338, 161

Gizis J. E., Reid I. N., Hawley S. L., 2002, AJ, 123, 3356

Gonzalez G., Carlson M. K., Tobin R. W., 2010, MNRAS, 403, 1368

Hatzes A. P. et al., 2000, ApJ, 544, L145

Herrero E., Ribas I., Jordi C., Guinan E. F., Engle S. G., 2012, A&A, 537, A147

Holmberg J., Nordström B., Anderson J., 2009, A&A, 501, 941

Jeffers S. V., Donati J.-F., 2008, MNRAS, 390, 635

Jeffers S. V., Donati J.-F., Alecian E., Marsden S. C., 2011, MNRAS, 411, 1301

Jeffers S. V., Petit P., Marsden S. C., Morin J., Donati J.-F., 2014, A&A, in press

Kochukhov O., Makaganiuk V., Piskunov N., 2010, A&A, 524, A5

Konstantinova-Antova R., Aurière M., Petit P., Charbonnel C., Tsvetkova S., Lèbre A., Bogdonovski R., 2012, A&A, 541, A44

Kupka F. G., Ryabchikova T. A., Piskunov N. E., Stempels H. C., Weiss W. W., 2000, Balt. Astron., 9, 590

Luck R. E., Heiter U., 2005, AJ, 129, 1063

Marcy G. W., Basri G, 1989, ApJ, 345, 480

Marsden S. C., Donati J.-F., Semel M., Petit P., Carter B. D., 2006, MNRAS, 370, 468

Marsden S. C. et al., 2011a, MNRAS, 413, 1922

Marsden S. C. et al., 2011b, MNRAS, 413, 1939

Martínez-Arnáiz R., Maldonado J., Montes D., Eiroa C., Montesinos B., 2010, A&A, 520, 79

Masana E., Jordi C., Ribas I., 2006, A&A, 450, 735

Mathys G., 1989, Fundam. Cosm. Phys., 13, 143

Mishenina T. V., Soubiran C., Kovtyukh V. V., Katsova M. M., Livshits M. A., 2012, A&A, 547, A106

Morgenthaler A. et al., 2012, A&A, 540, A138

Morin J. et al., 2008, MNRAS, 390, 567

Nidever D. L., Marcy G. W., Butler R. P., Fischer D. A., Vogt S. S., 2002, ApJS, 141, 503

Noyes R. W., Hartmann L. W., Baliunas S. L., Duncan D. K., Vaughan A. H., 1984, ApJ, 279, 763

Pace G., 2013, A&A, 551, L8

Parker E. N., 1955, AJ, 122, 293

Perryman M. A. C. et al., 1997, A&A, 323, L49

Petit P., Donati J.-F., the ESPaDOnS Project Team, 2003, in Arnaud J., Meunier N., eds, EAS Pub. Ser. Vol. 9, Magnetism and Activity of the Sun and Stars. p. 97

Petit P. et al., 2004, MNRAS, 348, 1175

Petit P. et al., 2005, MNRAS, 361, 837

Petit P. et al., 2008, MNRAS, 388, 80

Petit P., Dintrans B., Morgenthaler A., Van Grootel V., Morin J., Lanoux J., Aurière M., Konstantinova-Antova R., 2009, A&A, 508, L9

Petit P., Aurière M., Konstantinova-Antova R., Morgenthaler A., Perrin G., Roudier T., Donati J.-F., 2013, in Jean-Pierre R., Neiner C., eds, Lecture Notes in Physics, Vol. 857, The Environments of the Sun and the Stars. Springer-Verlag, Berlin, p. 231

Planck Collaboration I, 2013, preprint (arXiv:1303.5062)

Ramírez I., Allende Prieto C., Lambert D. L., 2007, A&A, 465, 271

Ramírez I., Meléndez J., Asplund M., 2009, A&A, 508, L17

Reiners A., 2012, Living Rev. Sol. Phys., 9, 1

Reiners A., Basri G., Browning M., 2009, ApJ, 692, 538

Saar S., 2002, in Favata F., Drake J. J., eds, ASP Conf. Ser. Vol. 277, Stellar Coronae in the Chandra and XMM-Newton Era. Astron. Soc. Pac., San Francisco, p. 311

Saar S. H., Baliunas S. L., 1992, in Harvey K. L., ed., ASP Conf. Ser. Vol. 27, The Solar Cycle. Astron. Soc. Pac., San Francisco, p. 197

Santos N. C., Israelian G., Mayor M., 2004, A&A, 415, 1153

Semel M., 1989, A&A, 225, 456

Shorlin S. L. S., Wade G. A., Donati J.-F., Landstreet J. D., Petit P., Sigut T. A. A., Strasser S., 2002, A&A, 392, 637

Soubiran C., Bienaymé O., Mishenina T. V., Kovtyukh V. V., 2008, A&A, 480 91

Strassmeier K. G., Fekel F. C., Bopp B. W., Dempsey R. C., Henry G. W., 1990, ApJS, 72, 191

Strassmeier K. G., Pichler T., Weber M., Granzer T., 2003, A&A, 411, 595

Takeda Y., Ohkubo M., Sato B., Kambe E., Sadakane K., 2005, Publ. Astron. Soc. Japan, 57, 27

Takeda G., Ford E. B., Sills A., Rasio F. A., Fischer D. A., Valenti J. A., 2007a, ApJS, 168, 297

Takeda Y., Kawanomoto S., Honda S., Ando H., Sakuri T., 2007b, A&A, 468, 663

Valenti J. A., Fischer D. A., 2005, ApJS, 159, 141

Valenti J. A., Marcy G. W., Basri G., 1995, ApJ, 439, 939

Vidotto A. A., Fares R., Jardine M., Donati J.-F., Opher M., Moutou C., Catala C., Gombosi T. I., 2012, MNRAS, 423, 3285

Waite I. A., Marsden S. C., Carter B. D., Petit P., Donati J.-F., Jeffers S. V., Boro Saikia S., 2014, MNRAS, submitted

Wenger M. et al., 2000, A&AS, 143, 9

Wielen R., 1962, AJ, 67, 599

Wright J. T., Marcy G. W., Butler R. P., Vogt S. S., 2004, ApJS, 152, 261

Wright N. J., Drake J. J., Mamajek E. E., Henry G. W., 2011, ApJ, 743, 48

Wu Y., Singh H. P., Prugniel P., Gupta R., Koleva M., 2011, A&A, 525, 71

Yoss K. M., Griffin R. F., 1997, J. Astrophys. Astron., 18, 161

APPENDIX A: NOTES ON INDIVIDUAL STARS

A1 HIP 16537 (ε Eri)

Epsilon Eridani is an active K-star (K2V according to the SIMBAD data base) and a possible planet-hosting star (Hatzes et al. 2000; Benedict et al. 2006; Butler et al. 2006; Anglada-Escudé & Butler 2012) and as such its magnetic field properties are of significant interest in the study of the impact of magnetic activity on the formation and evolution of orbiting planets. We have 58 observations of eps Eri with a vast majority (52) showing definite detections of a magnetic field. The star is very young, with an estimated age of 0.0–0.6 Gyr (according to Takeda et al. 2007a). The star is a slow rotator with a $v\sin i$ of 2.4 ± 0.4 km s^{-1} and shows a very strong B_1 (-10.9 ± 0.2 G) for such low rotational broadening (it is one of the stars above the line in Fig. 13). An individual map of eps Eridani is presented in Petit et al. (in preparation), while an analysis of the full data set (spanning five epochs of observations) is presented in Jeffers et al. (2014). The LSD profile of the star is shown in Fig. A1.
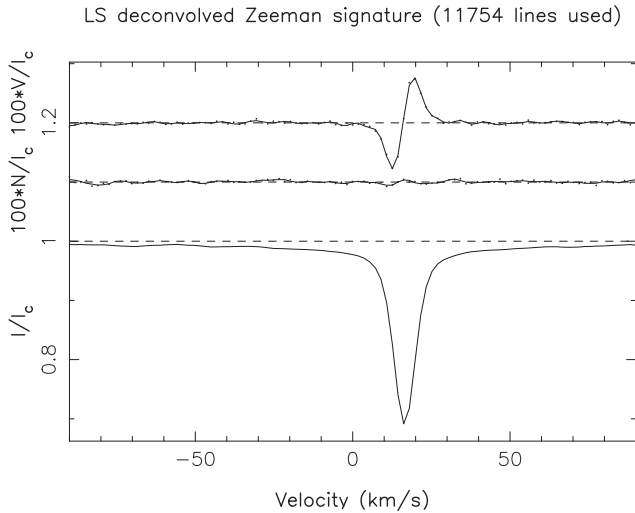
LS deconvolved Zeeman signature (11754 lines used)

Figure A1. Plot of the LSD profile for HIP 16537 (Epsilon Eri), with the upper plot showing the Stokes *V* LSD profile (expanded by 100 times and shifted up by 0.2), the middle plot showing the null LSD profile (again expanded by 100 times and shifted up by 0.1) and the lower plot showing the Stokes *I* LSD profile.

A2 HIP 71631 (EK Dra)

EK Dra is often described as an infant Sun (SIMBAD spectral type of G1.5V) with $T_{eff} = 5845 \pm 44$ K, a mass of $1.044^{+0.014}_{-0.020}$ M$_\odot$ and an age of 0.00–1.44 Gyr (Takeda et al. 2007a). It is one of the most rapidly rotating, and hence active, stars in our sample with $v\sin i = 16.8 \pm 0.5\,\mathrm{km\,s^{-1}}$ and $B_l = +45.3 \pm 2.8$ G. The LSD profile, showing its large Stokes *V* signature, is given in Fig. A2, and the magnetic maps of this star (using these observations) are presented in Waite et al. (in preparation), showing the evolution of the magnetic topology over several epochs of observations.

A3 HIP 79672 (18 Sco)

18 Scorpius is an interesting target as it is often proposed as one of the best solar twins among bright stars (SIMBAD spectral type of G2Va) with $T_{eff} = 5791 \pm 44$ K, $\log(g) = 4.42 \pm 0.03$ cm s^{-2},
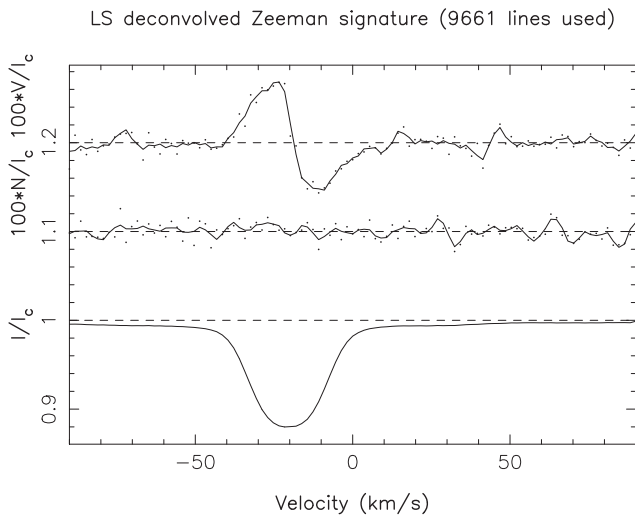
LS deconvolved Zeeman signature (9661 lines used)

Figure A2. Plot of the LSD profile for HIP 71631 (EK Dra), with the plots as described in Fig. A1.

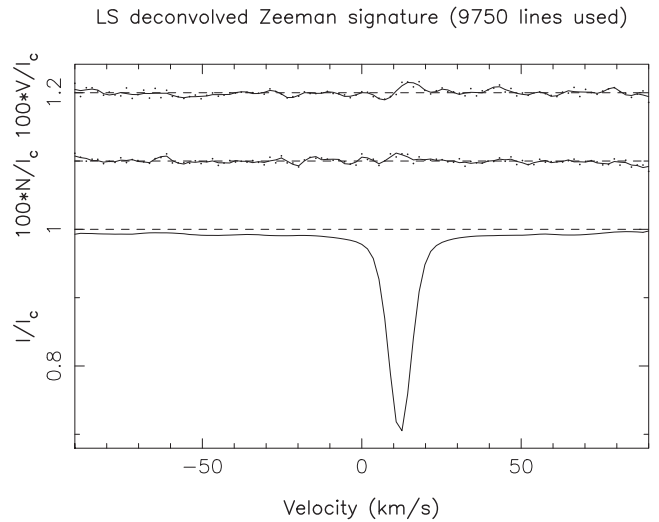LS deconvolved Zeeman signature (9750 lines used)

Figure A3. Plot of the LSD profile for HIP 79672 (18 Sco), with the plots as described in Fig. A1.

$\log(\mathrm{M/H}) = +0.03 \pm 0.03$, age $= 5.84^{+1.88}_{-1.96}$ Gyr, mass $= 1.005^{+0.028}_{-0.024}$ and $v\sin i = 2.6 \pm 0.5\,\mathrm{km\,s^{-1}}$. We have 57 observations of 18 Sco, but only 12 have resulted in marginal or definite detections of a polarized signature. The maximum measured value of B_l is only a few gauss (-2.3 ± 0.4 G) and as can be seen in Fig. A3, the strength of the magnetic signal in the Stokes *V* LSD profile is very weak. 18 Sco is very close to the limit of our observational capabilities with an S-index of 0.1834 at the epoch of the observation illustrated here. The magnetic topology of 18 Sco has previously been published (using the observations presented here) by Petit et al. (2008).

A4 HIP 91043 (V889 Her)

V889 Her is a young (age 30–50 Myr; Strassmeier et al. 2003) and active G-star (SIMBAD spectral type G2V). With the exception of its low metallicity ($\log(\mathrm{M/H}) = -0.5$), V889 Her could well be considered an active young Sun and is typical of the active stars more frequently observed using spectropolarimetry. Given its youthfulness and rapid rotation ($v\sin i = 39.0 \pm 0.5\,\mathrm{km\,s^{-1}}$), it is unsurprising that we have a large number of magnetic field detections for the star (48 out of 53 observations are definite detections). The maximum measured mean longitudinal field is significantly higher than that seen on the more mature (and less rapidly rotating) solar-type stars with a value of $+89.7 \pm 12.2$ G. The LSD profile of the star is given in Fig. A4 while numerous magnetic field maps of the star have been previously published (Marsden et al. 2006; Jeffers & Donati 2008; Jeffers et al. 2011). Additionally, because of its large $v\sin i$, the spot features of V889 Her can also be mapped using Doppler imaging and have also been published in the above-mentioned papers.

A5 HIP 104214 (61 Cyg A)

61 Cyg A is one of the coolest stars in our sample (along with ξ Boo B) with $T_{eff} = 4525 \pm 140$ K, is very young (an age of 0.00–0.44 Gyr) and has a small $v\sin i$ value ($\sim$1.1 km s^{-1}). The star's SIMBAD spectral type is given as K5V. 68 observations of 61 Cyg A have been obtained with over two-thirds (49) showing marginal or definite detections of a surface magnetic field. The maximum measured value of B_l is quite high (-8.9 ± 0.3 G) given its low
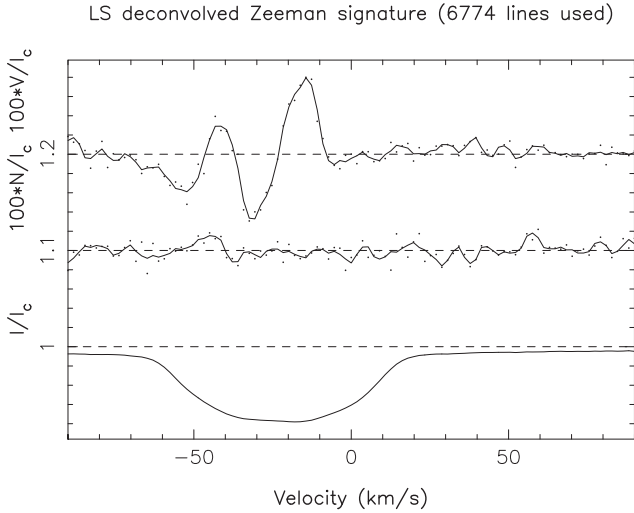
Figure A4. Plot of the LSD profile for HIP 91043 (V889 Her), with the plots as described in Fig. A1.
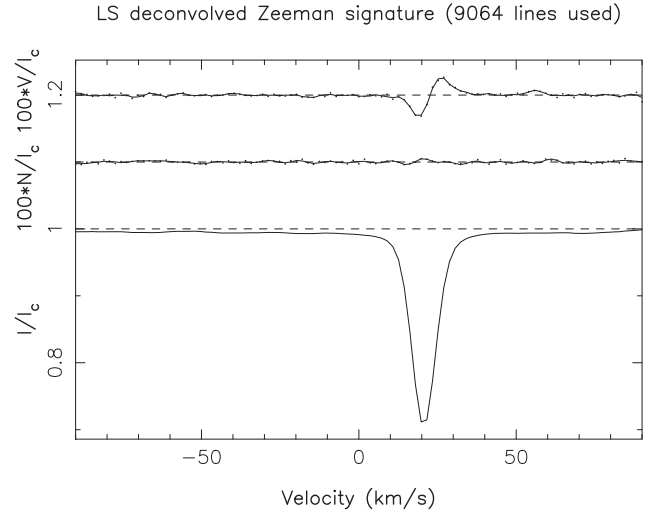

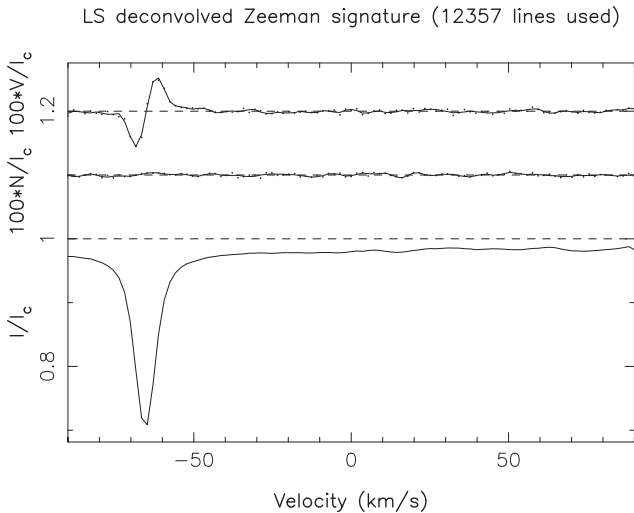**Figure A6.** Plot of the LSD profile for HIP 109439, with the plots as described in Fig. A1.

Figure A5. Plot of the LSD profile for HIP 104214 (61 Cyg A), with the plots as described in Fig. A1.

Figure A7. Plot of the LSD profile for HIP 113357 (51 Pegase), with the plots as described in Fig. A1.

$v \sin i$. The LSD profile of the star is given in Fig. A5, and a map of the magnetic topology of the star is given in Petit et al. (in preparation).

A6 HIP 109439

HIP 109439 is an interesting target as it is a subgiant member of our sample, with $T_{\mathrm{eff}} = 5658 \pm 44$ K, $\log(g) = 3.79^{+0.04}_{-0.02}$ cm s^{-2}, a mass of $1.49^{+0.23}_{-0.20}$ M$_\odot$ and a radius of $2.95^{+0.11}_{-0.02}$ R$_\odot$. Most observed subgiant stars are low-activity objects, as can be seen in their Ca II H&K measurements (see Table 6), although HIP 109439 is moderately active with $\log(R'_{\mathrm{HK}}) = -4.72$. The Stokes V LSD profile of HIP 109439 is given in Fig. A6. From our single observation, we obtain a definite detection of a surface magnetic field. The estimated mass suggests that HIP 109439 may be the descendant of a main-sequence star with a very shallow convective envelope, so that the generation of a detectable large-scale magnetic field may be relatively recent and linked to the growth of its post-main-sequence convective envelope.
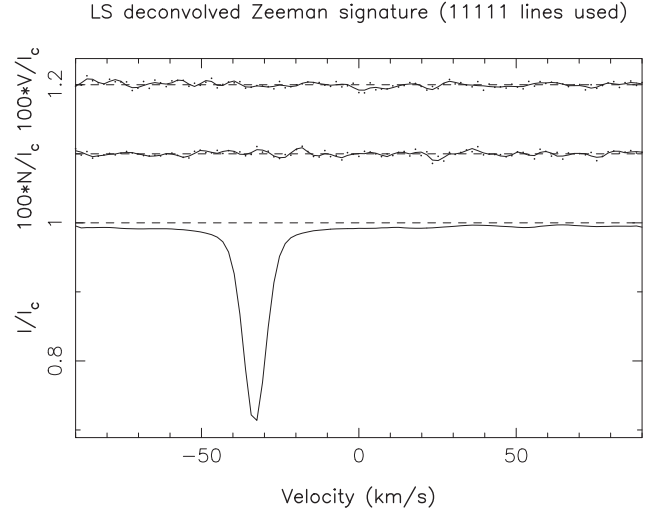
A7 HIP 113357 (51 Pegase)

51 Pegasi was the first Sun-like star (the SIMBAD spectral type is given as G2.5IVa) to be found to have a planetary companion. 51 Peg has similar properties to that of our own Sun with $T_{\mathrm{eff}} = 5787 \pm 25$ K, $\log(\mathrm{M/H}) = +0.15 \pm 0.02$, $v \sin i = 2.6 \pm 0.3$ km s^{-1} and an age of $\sim$7 Gyr. The age and slow rotation rate of the star make it a challenging target for spectropolarimetry and unfortunately we have no detections of a magnetic field in the three observations we have for the star. The largest magnetic field we have been able to estimate on the star is $B_{\mathrm{l}} = +0.6 \pm 0.4$ G. The LSD profile of the star is given in Fig. A7.

A8 HIP 113994

Like HIP 109439 (see Section A6) HIP 113994 is classified by us as a subgiant star with $T_{\mathrm{eff}} = 5301 \pm 44$ K, $\log(g) = 3.96^{+0.02}_{-0.01}$ cm s^{-2}, a mass of 2.02 ± 0.31 M$_\odot$ and a radius of $2.48^{+0.02}_{-0.09}$ R$_\odot$. The SIMBAD spectral type for the star is given as G8IV. We have only one observation of this star, corresponding to a definite detection
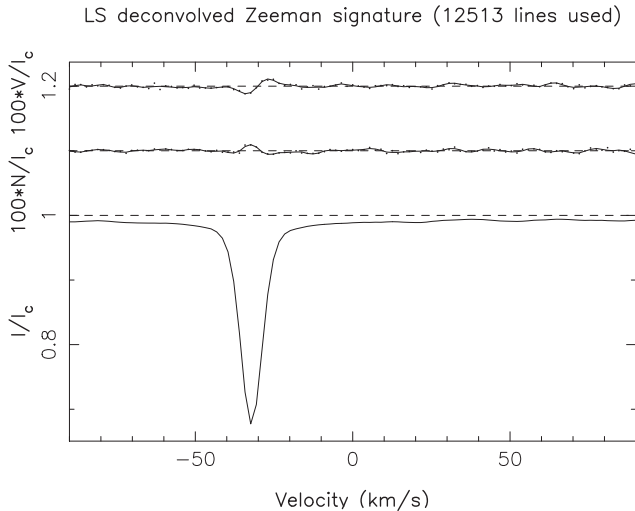
Figure A8. Plot of the LSD profile for HIP 113994, with the plots as described in Fig. A1.

Figure A9. Plot of the LSD profile for HIP 114378, with the plots as described in Fig. A1.

(FAP = 2.243 × 10^{-14}) of a surface magnetic field, in spite of its rather low log(R'_{HK}) value of −5.04. The star only just has a log(g) below 4.0 cm s^{-2} but the mass and radius, compared to its effective temperature, would indicate that this is a subgiant star worthy of further study, since it may be the descendant of a main-sequence star too massive to have deep convective outer layers, and therefore not suited to generate an efficient solar-type dynamo. The Stokes V profile of the star is given in Fig. A8. We also record a bump in the null profile (with an amplitude smaller than that of the Stokes V profile), so that the star should be re-examined to determine if this detection can be confirmed.

A9 HIP 114378

HIP 114378 is listed in Table 1 as a G-star (SIMBAD spectral type of G0V) with a mass near solar, an age of ∼7 Gyr and a $v\sin i$ of ∼10 km s^{-1}. The star has been observed twice, with both observations yielding definite detections. The star is slightly unusual in that the magnetic field measured (B_l) is rather strong (−11.1 ± 1.8 G) for its age, as derived from evolutionary tracks. Using equation 13 from Wright et al. (2004) gives an age of 0.22–0.35 Gyr, based on the range of its log(R'_{HK}) values (Table 6). If the evolutionary age of Takeda et al. (2007a) is correct, the high activity of this star may indicate that the star is a member of a close binary system, although no evidence of a secondary companion is seen in its Stokes I LSD profile (Fig. A9). The null profile of this star shows a statistically significant signature in the line profile, but the variations in the Stokes V LSD profile are well above those seen in the diagnostic profile. We therefore consider the magnetic field detection to be robust, although error bars on B_l may be underestimated.

A10 HD 131156A and B (ξ Boo A and B)

The ksi Boo system is a very long-period binary (orbital period ∼151 yr; Wielen 1962) with the A component being an active G-star (SIMBAD spectral type of G8V) while the B component is an active K-star (SIMBAD spectral type of K4V). Ksi Boo A has been studied previously as part of the BCool solar-type star project (Morgenthaler et al. 2012) with magnetic topologies reconstructed for seven different epochs from 2007 to 2011, showing magnetic field evolution but with no cycle yet determined. The age of the
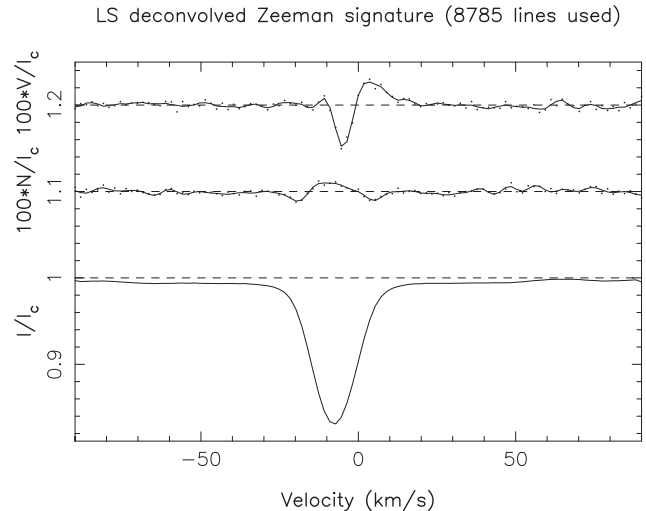
two components of the system (according to Takeda et al. 2007a) is markedly different (0.00–0.76 Gyr for A and 12.60–13.80 Gyr for B), but given the activity of the two components, the system is most likely young, with the activity-based ages from Wright et al. (2004) being 0.00–0.35 Gyr for A and 0.18–3.89 Gyr for B, based on the range of their log(R'_{HK}) values (Table 6). The radii and masses of the system (again determined by Takeda et al. 2007a) are very similar (with B being slightly higher than A) despite their significant temperature differences, as thus the derived parameters for these two stars should be treated with caution. Both stars gave definite detections for surface magnetic fields, and the LSD profiles of these stars are given in Fig. A10. A magnetic map of ksi Boo B is given in Petit et al. (in preparation).

A11 The Moon

We use here an observation of solar light reflected on the moon as a proxy of a Sun-as-a-star spectropolarimetric observation. The low activity of the Sun makes it a difficult target for spectropolarimetry and although the LSD profile (Fig. A11) shows a small bump in Stokes V (along with a small dip in the null parameter) we did not get a magnetic detection for our only spectrum.

APPENDIX B: SUMMARY OF SPECTROPOLARIMETRIC OBSERVATIONS

As mentioned previously (Section 3), the data for this project have been obtained during 25 observing runs at the TBL and CFHT using the NARVAL and ESPaDOnS spectropolarimeters, respectively. The observations were obtained from late-2006 through to mid-2013 with the majority of the observing runs (19/25 = 76 per cent) being carried out at the TBL. The majority of the targets have only been observed once (117/170 = 69 per cent) or at only one epoch of observations (135/170 = 79 per cent); however, a number of stars have been observed at multiple epochs to look for temporal evolution in their magnetic field properties. These stars will be the subjects of forthcoming BCool papers. A summary of the number of observations for each star at each observing epoch is given in Table B1.
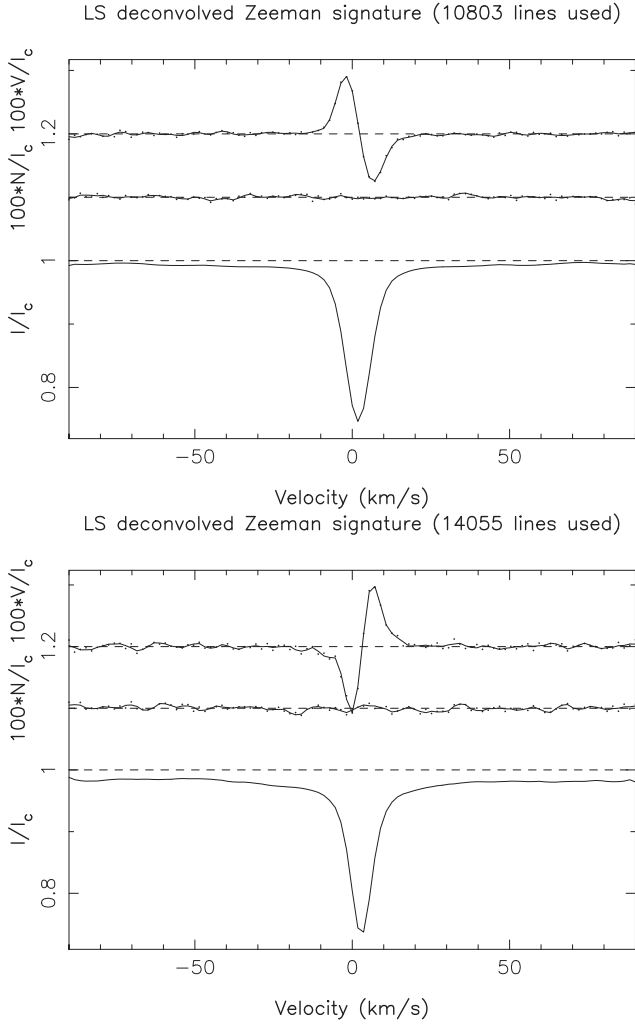
LS deconvolved Zeeman signature (10803 lines used)

LS deconvolved Zeeman signature (14055 lines used)

Figure A10. Plot of the LSD profile for ξ Boo system, HD 131156A (top) and HD 131156B (bottom), with the plots as described in Fig. A1.

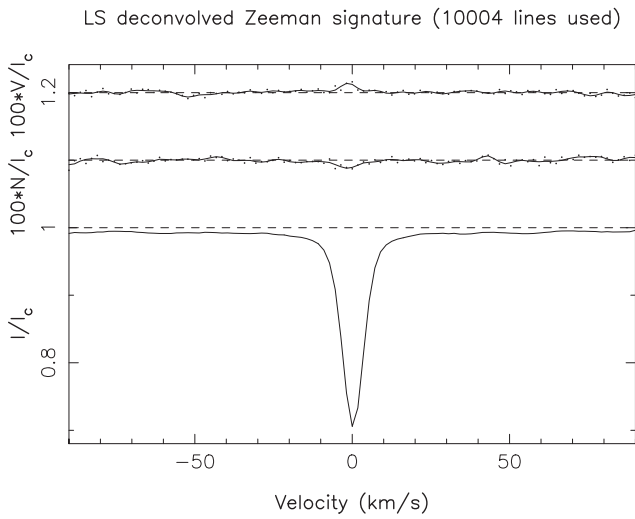LS deconvolved Zeeman signature (10004 lines used)

Figure A11. Plot of the LSD profile for the Moon, with the plots as described in Fig. A1.

Table B1. Summary of the number of observations of each star at each observing epoch in the BCool solar-type stars sample. The top section of the table lists the telescope used (TBL: Télescope Bernard Lyot, CFHT: Canada–France–Hawaii Telescope) and the year, start month and end month of the observations. ^SG.: identifies the star as a subgiant, see Fig. 1. The complete version of this table is in the electronic edition of the journal. The printed edition contains only a sample.

Telescope:	TBL	CFHT	TBL	TBL	TBL	TBL	CFHT	TBL	TBL	CFHT	CFHT	CFHT	TBL	TBL	TBL	CFHT	TBL	TBL	TBL	CFHT	TBL	TBL	TBL	TBL	TBL
Year (2000+):	06	06	07/08	07	07	07	07	07/08	08	08	08	08	08	09	09	09/10	09/10	10	10/11	11	11	11/12	12	12/13	13
Start:	Nov.	Nov.	June	May	July	Nov.	Dec.	Dec.	Jan.	March	May	June	July	Jan.	May	Sept.	Dec.	March	Sept.	Feb.	March	Oct.	March	Oct.	March
End:	Nov.	Dec.	Feb.	May	Aug.	Nov.	Dec.	Jan.	Feb.	March	May	July	Aug.	Jan.	July	Jan.	Feb.	Aug.	Feb.	July	Aug.	Feb.	Aug.	Jan.	Aug.
HIP #																									
400	—	—	—	—	—	—	—	—	—	—	—	—	—	—	—	—	—	—	1	—	—	—	—	—	—
544	—	—	—	—	—	—	—	—	—	—	—	—	—	—	—	—	—	—	1	—	—	—	—	—	—
682	—	—	—	—	—	—	—	—	—	—	—	—	—	—	—	—	—	—	1	—	—	—	—	—	—
1499	—	—	—	—	—	—	—	—	—	—	—	—	—	—	—	—	—	—	1	—	—	—	—	—	—
1813	—	—	—	—	—	—	—	—	—	—	—	—	—	—	—	—	—	—	1	—	—	—	—	—	—
...																									

SUPPORTING INFORMATION

Additional Supporting Information may be found in the online version of this article:

 (http://mnras.oxfordjournals.org/lookup/suppl/doi:10.1093/mnras/stu1663/-/DC1).

Please note: Oxford University Press are not responsible for the content or functionality of any supporting materials supplied by the authors. Any queries (other than missing material) should be directed to the corresponding author for the article.

This paper has been typeset from a TEX/LATEX file prepared by the author.